Summer 5-12-2017

MODELING ATMOSPHERE-MOUNTAIN INTERACTIONS: IMPLICATIONS FOR STABLE ISOTOPE-BASED PALEOALTIMETRY

Lauren B. Wheeler
University of New Mexico

Lauren Bronwyn Wheeler
Candidate

Earth and Planetary Sciences Department
Department

This dissertation is approved, and it is acceptable in quality and form for publication:

Approved by the Dissertation Committee:

Dr. Joseph Galewsky, Chairperson

Dr. Brandon Schmandt

Dr. Lindsay Lowe Worthington

Dr. John Wakabayashi

MODELING ATMOSPHERE-MOUNTAIN INTERACTIONS: IMPLICATIONS FOR STABLE ISOTOPE-BASED PALEOALTIMETRY

by

LAUREN BRONWYN WHEELER

M.Sc. Earth and Climate Sciences, University of Maine, 2013
B.S. Earth Sciences, University of Maine, 2011

DISSERTATION

Submitted in Partial Fulfillment of the Requirements for the Degree of

Doctor of Philosophy in Earth and Planetary Sciences

**The University of New Mexico
Albuquerque, New Mexico**

JULY 2017

ACKNOWLEDGEMENTS

The research in this dissertation was made possible with the help of many others. I would first like to thank my committee, Joseph Galewsky, Lindsay Lowe Worthington, Brandon Schmandt, and John Wakabayashi for their help and support. I would also like to thank Matthew Huber and Nicholas Herold, who are coauthors on Chapter 2.

Each chapter of this dissertation greatly benefited from publicly available climate data, models, and computing resources. High-performance computing support was supplied by the National Center for Atmospheric Research (NCAR) and the University of New Mexico's Center for Advanced Research Computing (CARC). All of the real and idealized simulations in Chapters 2 through 4 were run on NCAR's Yellowstone or CARC's Gibbs supercomputers. NCAR and CARC also provided storage for the simulations run for this dissertation. North American Regional Reanalysis (NARR) output (http://www.esrl. noaa.gov/psd/) from the Earth System Research Laboratory Physical Science Division was used for the modern climate data in Chapter 2. The simulation of Miocene climate in Chapter 2 was supplied by Nicholas Herold and Matthew Huber. NCEP FNL Operational Model Global Tropospheric Analyses (NCEP FNL), a product of the National Centers for Environmental Prediction/National Weather Service/NOAA/U.S. Department of Commerce, was used in Chapter 4. Both the NARR and NCEP FNL climate data were obtained through the Research Data Archive at NCAR. The Weather Research and Forecasting (WRF) model was used extensively in this dissertation to model both real and idealized simulations of the atmosphere. For trajectory analyses of real WRF simulation output, the HYSPLIT transport and dispersion model provided by the NOAA Air Resources Laboratory was used in Chapter 4. For trajectory analyses of idealized WRF output, Read/Interpolate/Plot version 4.6 (www2.mmm.ucar.edu/mm5/WRF_post/RIP4.htm) was used in Chapter 2.

While fieldwork was not necessary for the completion of this dissertation, I was granted several opportunities to experience international and domestic field sites. I would like to thank Joseph Galewsky for supporting these experiences and providing the opportunity to travel internationally and collect data in the field at the Chajnantor Plateau and along the Kali Gandaki. I would like to thank John Wakabayashi for leading me on a field trip in the Sierra Nevada so that I could experience the geologic sites for myself.

Financial support was generously provided for my graduate studies from a National Science Foundation grant awarded to Joseph Galewsky (EAR 1049903) along with generous scholarship support from the Department of Earth and Planetary Sciences and the Graduate and Professional Student Association.

Lastly, I would like to thank the graduate students in the Earth and Planetary Sciences Department for their friendship and constructive feedback throughout my time here. An especially big thanks goes out to the following: the other Lauren, Marisa, Rachel, Jordan, Margaret, Tori, Charlie, Mark, Carmen, and Kym!

MODELING ATMOSPHERE-MOUNTAIN INTERACTIONS: IMPLICATIONS FOR STABLE ISOTOPE-BASED PALEOALTIMETRY

by

LAUREN BRONWYN WHEELER

Ph.D., Earth and Planetary Sciences, University of New Mexico, 2017
M.Sc. Earth and Climate Sciences, University of Maine, 2013
B.S. Earth Sciences, University of Maine, 2011

ABSTRACT

The measure of surface uplift can provide an important constraint on the behavior of continental lithosphere and the underlying upper mantle. Isotope-based paleoaltimetry aims to quantitatively estimate the magnitude and timing of surface uplift from records of the isotopic composition of precipitation in order to provide constraints on the tectonic processes driving mountain building. As the surface of a topographic barrier increases in height, along the windward side, δ-values of precipitation should get progressively more negative, and on the leeside, δ-values of precipitation should also get progressively more negative based on the presence and development of a topographically-induced rain shadow. If modern precipitation and the isotopic composition of that precipitation are indeed related to the elevation of the mountain range, a record of paleo-δ-values should, in principle, contain a record of the paleoelevation.

A deeper understanding of the processes that control the windward and leeside isotopic composition of precipitation will improve interpretations of isotope-based paleoaltimetry records and has the potential to improve the reliability of the technique for constraining the topographic and tectonic evolution of mountain ranges. In this study I

focus on the underlying assumptions within isotope-based paleoaltimetry interpretations from windward and leeside studies, for both empirical and theoretical approaches. The research presented here focuses on: (1) the role of atmospheric flow deflection on leeside isotope-based paleoaltimetry records and the subsequent interpretations of those records in the southern Sierra Nevada and the Southern Alps (Chapter 2 and Chapter 4), (2) whether simple models of upslope flow are sufficient for understanding mountain-atmosphere interactions (Chapter 3), and (3) the limitations and opportunities provided by theoretical approaches based on Rayleigh distillation (Chapter 3).

Through the comparison of leeside isotope-based paleoaltimetry in the southern Sierra Nevada and the Southern Alps, I conclude that leeside isotope-based paleoaltimetry is best applied in relatively low-lying mountain ranges with simple uplift histories, and where atmospheric flow patterns are primarily two-dimensional (Chapter 2 and Chapter 4). From simulations of windward lapse rates for orographically enhanced precipitation, I find that lapse rates generally steepen with increasing elevation and lapse rates from Rayleigh distillation models are almost always steeper than the simulated lapse rates due to the high precipitation efficiency (Chapter 3). The difference in lapse rates between Rayleigh distillation models and the simulations of orographic precipitation suggests that Rayleigh distillation models may be best used for determining the minimum elevation of a mountain range and the maximum amount of uplift.

PREFACE

The purpose of this preface is to outline the role of each coauthor in multi-author papers included in this dissertation in accordance with the Department of Earth and Planetary Sciences' guidelines. Chapter 2 of this dissertation was published in Geology after undergoing the peer-review process. Chapters 3 and 4 are in preparation for submission to Geology. Lauren B. Wheeler is the primary author of, and conducted more than 51% of the work for, each manuscript.

Chapter 2 focuses on atmospheric flow deflection in the southern Sierra Nevada due to changes in climate and elevation and the implications this has for leeside isotope-based paleoaltimetry interpretations. Joseph Galewsky provided guidance through all aspects of this project. Idealized simulations of atmospheric flow, trajectory analysis, and analysis of modern climate data were conducted by Lauren Wheeler. Paleoclimate models were run by Nicholas Herold (University of New South Wales, Sydney, Australia) as a post-doc with Matthew Huber (University of New Hampshire, Durham, New Hampshire).

Chapter 3 focuses on windward isotope-based paleoaltimetry through simulations of orographically enhanced precipitation. Specifically, how lapse rates change with increasing elevation and whether Rayleigh distillation models sufficiently reproduce simulated lapse rates. Modifications to the Weather Research and Forecasting (WRF) model, model testing, simulations of atmospheric flow, and all analyses were the work of Lauren Wheeler. Joseph Galewsky provided guidance through all aspects of this project.

Chapter 4 focuses on atmospheric flow deflection in the Southern Alps of New Zealand and whether leeside paleo-isotope records would likely record the uplift of the

Southern Alps. The down-scaled climate simulations, trajectory analysis, and atmospheric analyses were done by Lauren Wheeler. Joseph Galewsky provided guidance through all aspects of this project.

TABLE OF CONTENTS

TABLE OF FIGURES

1. INTRODUCTION

Since the early 1990s there has been an increased interest in understanding the relationship between tectonics and the topography of global mountain ranges (Merritts and Ellis, 1994). Topography is the result of the interaction of many different processes (e.g. tectonics, climate, surface processes) and can yield insight into the tectonic evolution of a mountain range. Due to the complexity of these interactions though, it is not always easy to establish the timing and magnitude of topographic evolution. There are 3 types of uplift; surface uplift, exhumation, and rock uplift. Surface uplift is the change in elevation for the boundary between the atmosphere and Earth's surface, over a broad region (10^3-10^4 km^2), relative to the geoid, rock uplift is the displacement of rocks with respect to the geoid, and exhumation is the displacement of rocks with respect to the surface (England and Molnar, 1990). Surface uplift, exhumation, and rock uplift are all related in the following equation: surface uplift = rock uplift – exhumation. In cases where the surface uplift is not explained simply by crustal thickening, the measure of surface uplift can provide an important constraint on the behavior of continental lithosphere and the underlying upper mantle (England and Molnar, 1990; Molnar and Lyon-Caen, 1988).

As of 1990, there was no reliable, quantitative means of estimating rates of surface uplift in mountain ranges needed to place useful constraints on tectonic processes (England and Molnar, 1990). Through techniques such as geobarometery, geothermometry, and cooling age studies, rates of exhumation can be quantified but not necessarily rates of surface uplift (England and Molnar, 1990). Sedimentological records can occasionally provide quantitative estimates on rates of surface uplift but this requires a very specific setting, such as well-dated coastal terraces in tectonically active settings (e.g. Abbott et al., 1996). Isotope-based paleoaltimetry was developed as a way to quantitatively estimate the magnitude and timing of surface uplift from records of the isotopic composition of precipitation in order to provide constraints on the tectonic processes driving mountain building.

1.1. Isotope-based paleoaltimetry

Dansgard (1964) first recognized that there was a relationship between the isotopic composition of precipitation and altitude. Where as altitude increases, $\delta^{18}O$ and δD (from here on referred to as δ-values) decrease as a result of cooler temperatures, which leads to greater fractionation. This behavior is evidenced by a compilation of δ-values from waters along the windward side of global mountain ranges (Figure 1.1) (Chamberlain and Poage, 2000). Orographic precipitation is thought to be the main driver of these isotopic patterns: as an air mass is lifted along the windward side of a mountain range, water vapor condenses due to decreasing temperatures with altitude, and the heavier isotopes are preferentially rained out. With increasing elevation and as the air mass reaches the leeside, δ-values are increasingly more negative (Figure 1.2). If modern precipitation and the isotopic composition of that precipitation are indeed related to the elevation of the mountain range, a record of paleo-δ-values should, in principle, contain a record of the paleoelevation. This is the premise for both windward and leeside isotope-based paleoaltimetry studies.

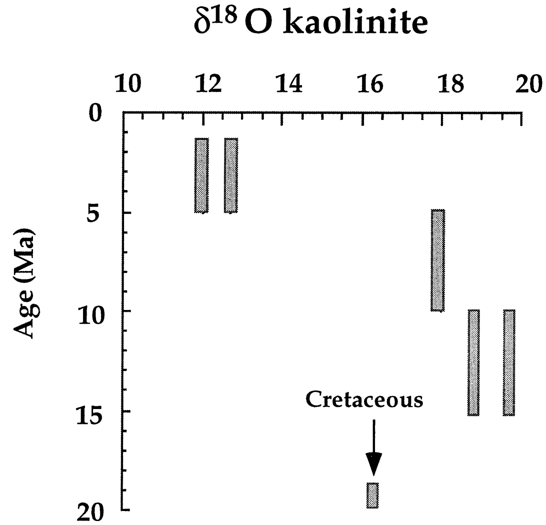

Figure 1.1. $\delta^{18}O$ of kaolinite collected on the leeside of the Southern Alps of New Zealand. Figure from Chamberlain et al. (1999). The decrease in $\delta^{18}O$ at 5 Ma is interpreted as the onset of aridification with the development of the Southern Alps.

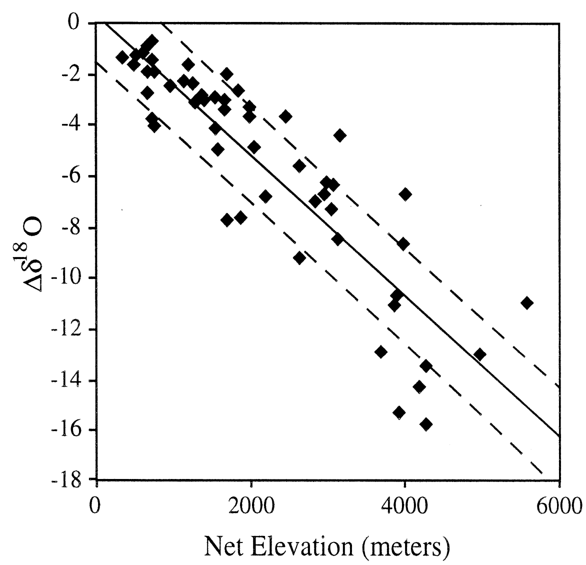

Figure 1.2. Global compilation of $\Delta\delta^{18}O$ versus net elevation. Figure from Poage and Chamberlain (2001). Lapse rates from waters along the windward face of global mountain ranges are roughly consistent globally at -2.8 ‰/km for $\delta^{18}O$ ($r^2 = 0.8$).

Taylor (1974) suggested that the isotopic composition of meteoric waters could be preserved in kaolinites and other geologic materials. Although it wasn't until Chamberlain et al. (1999) that the use of isotope-based paleoaltimetry began to be used more extensively, Winograd et al. (1985) are the first to suggest that the δ-values from precipitation in a mountain range could be used to reconstruct the surface uplift history. Winograd et al. (1985) proposed that the changes in the isotopic composition of meteoric waters preserved in calcite veins in the Sierra Nevada were related to changes in elevation. Since Winograd et al. (1985) and Chamberlain et al. (1999) there have been numerous studies of paleoelevation using both windward and leeside isotope-based paleoaltimetry techniques. As the surface of a topographic barrier increases in height (surface uplift), along the windward side, δ-values of precipitation should get progressively more negative, and on the leeside, δ-values of precipitation should also get progressively more negative based on the presence and development of a topographically-induced rain shadow. Chamberlain et al. (1999) collected samples along the leeside of the Southern Alps of New Zealand and found a 5-6‰ decrease in $\delta^{18}O$ in authigenic kaolinite around 5 Ma. Their results suggest that a rain shadow developed around 5 Ma and that prior to this time the Southern Alps were a relatively low topographic feature (Figure 1.3). These results agree well with other lines of geologic evidence that suggest that the modern tectonic regime and uplift in the Southern Alps evolved over the last ~5 Ma (Sutherland, 1995; Walcott, 1998; Batt et al., 2000).

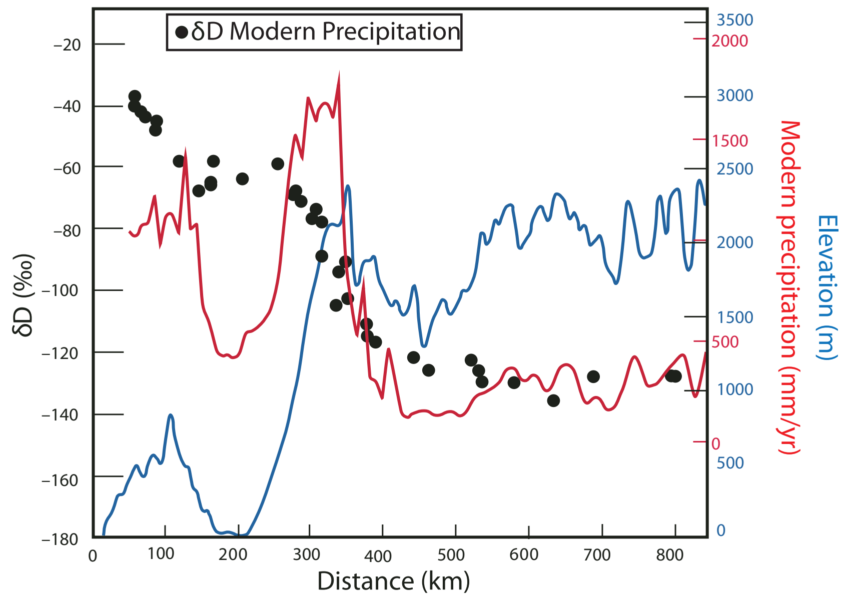

Figure 1.3. Topography (blue), modern precipitation in mm/yr (red), and δD of modern precipitation (from Ingraham and Taylor, 1991) across the northern Sierra Nevada. Figure modified from Mulch (2006). Along the profile, as elevation increases in the Sierra Nevada, precipitation increases and the δD of modern precipitation decreases by ~-40 ‰ across the range crest and another ~-50 ‰ into the leeside.

Chamberlain and Poage (2000) followed up the work of Chamberlain et al. (1999) with a compilation of the isotopic composition of waters along the windward side of global mountain ranges. Since there Chamberlain and Poage (2000) found that there was a good relationship between elevation and the isotopic composition of precipitation globally and the technique worked well in the Southern Alps, Chamberlain and Poage (2000) used leeside isotope-based paleoaltimetry to the Sierra Nevada. The evolution of the Sierra Nevada is a key piece of the tectonic evolution of the western United States and constraining surface uplift rates could provide useful constraints on the forces driving mountain building in the western United States. Both windward and leeside isotope-based paleoaltimetry have been used extensively in the northern and southern Sierra Nevada. Studies using leeside isotope-based paleoaltimetry are simply looking for a shift in δ-values with time that would indicate the establishment of a leeside rain shadow. Studies using windward isotope-based paleoaltimetry are slightly more complicated as they need to establish a modern lapse rate and a paleo-lapse rate along the windward face of the range to compare their records to.

Studies of windward isotope-based paleoaltimetry typically use either empirically- or theoretically-based methods to reconstruct paleoelevation. The empirical approach relies on modern global observations of the isotopic composition of waters and elevation. Lapse rates from waters along the windward face of global mountain ranges are roughly consistent globally at -2.8 ‰/km for $\delta^{18}O$, although with wide scatter (Poage and Chamberlain, 2001). If the lapse rate from the paleo-δ-values is steeper than modern elevations, the elevation at that time is interpreted to be higher than the modern elevation. If the lapse rate from the paleo-δ-values is shallower, the elevation at that time is interpreted to be lower than modern elevations. For example, Cassel et al. (2009) used a local empirically based lapse rate of -17.4 ‰/km (Ingraham and Taylor, 1991) for Cenozoic estimates of the paleoelevation of the northern Sierra Nevada. The paleo-δ-values, dated to the Eocene, had a steeper or similar-to-modern lapse rate, which suggested that the northern Sierra Nevada have been high since the Eocene.

Theoretical approaches rely on 1-D thermodynamic models of Rayleigh distillation to determine the change in δ-values with elevation for a given temperature profile and mixing ratio as an air parcel ascends (Rowley et al., 2001). Hren et al. (2010), use a Rayleigh distillation model, where temperature and relative humidity for different paleoclimates were used as inputs to determine the paleo-lapse rates for Eocene elevation reconstructions in the northern Sierra Nevada. They too found that the paleo-lapse rates were similar-to-modern, which again suggests that the elevation of the Eocene Sierra Nevada was either steeper or similar-to-modern.

1.2 Application of isotope-based paleoaltimetry to the Sierra Nevada

In both the northern and southern Sierra Nevada the interpretations of the uplift history from isotope-based paleoaltimetry (e.g. Cassel et al., 2009; Chamberlain and Poage, 2000; Mulch, 2016) conflict with other lines of geologic evidence (e.g. Wakabayashi, 2013). In the northern Sierra Nevada, isotope-based paleoaltimetry records have been used to suggest that the Eocene northern Sierra Nevada were either steeper than modern elevations or similar-to-modern elevations (Figure 1.4) (Hren et al., 2010; Cassel et al., 2009; Mulch et al., 2006, 2008). These isotope records come from several different proxies; volcanic glass (Cassel et al., 2009), plant leaf waxes (Hren et al., 2010), and kaolinite (Mulch, 2006), that range in date from the Eocene through the Pleistocene. However, the results from each of these studies contradict several other lines of geologic evidence. Wakabayashi (2013) discusses this in great detail but to summarize, paleo-channel azimuth-gradient relationships, erosion and stream incision, and the relationship between faulting and late Cenozoic volcanic deposits support late Cenozoic surface uplift in the northern Sierra Nevada and suggests that the Eocene northern Sierra Nevada was likely lower in elevation relative to the modern Sierra Nevada.

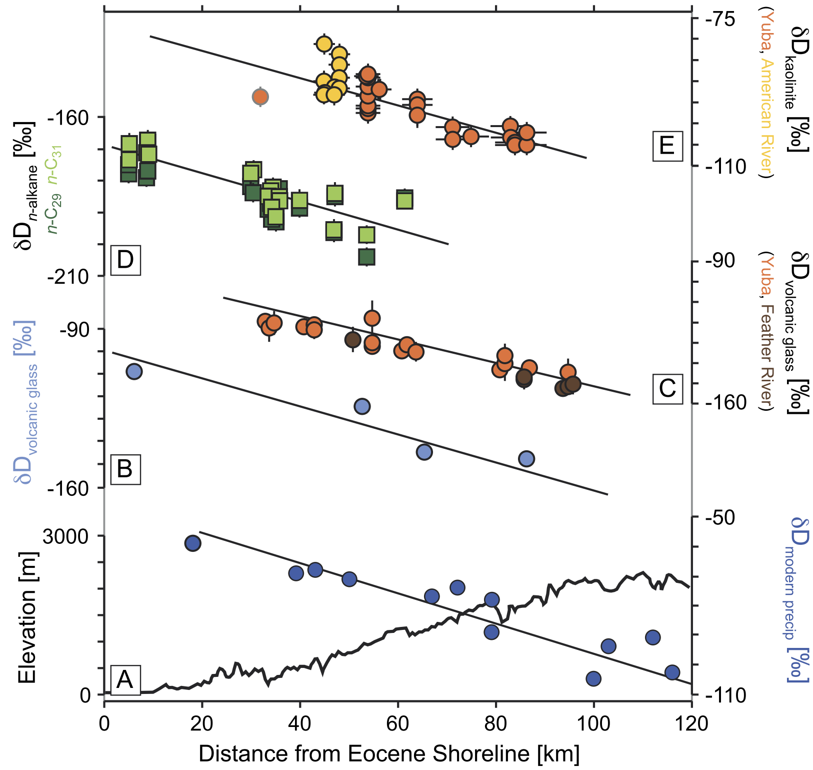

Figure 1.4. Records of paleo-meteoric (E-B) and modern (A) waters along the northern Sierra Nevada from the Eocene to Pleistocene (E-B) from records of authigenic (kaolinite), plant-derived (leaf wax n-alkanes) and hydrated (volcanic glass) proxy materials. Adapted from (A) Ingraham and Taylor (1991), (B) Mulch et al. (2008), (C) Cassel et al. (2009), (D) Hren et al. (2010), (E) Mulch et al. (2006). Figure from Mulch (2016).

In the southern Sierra Nevada isotope-based paleoaltimetry records initially suggested that the southern Sierra Nevada have been a long-standing feature since ~16 Ma (Figure 1.5) (Chamberlain and Poage, 2000). Clark et al. (2005) and Wakabayashi (2013) proposed two pulses of surface uplift in the southern Sierra Nevada over the last 20 Ma. The first pulse may have been driven by the opening of a slab window during the northward migration of the Mendocino triple junction (Wakabayshi, 2013). The event began in the southern most river drainages in the Sierra Nevada ~20 Ma, migrated ~130 km northward through the San Joaquin River drainage between 10-6 Ma, and then another ~100 km northward through the Mokelumne and Stanislaus River drainages around 4–3.6 Ma (Mahéo et al., 2009). The second pulse was relatively synchronous between the southern Sierra Nevada river basins and may have been driven by the delamination of high-density material beneath the southern Sierra Nevada post-3.6 Ma (Ducea and Saleeby, 1996). More recent interpretations of leeside isotope records suggest that a pattern of atmospheric flow deflection around the southern Sierra Nevada was established 12.1 Ma and as a result the southern Sierra Nevada was sufficiently high to induce similar-to-modern flow patterns since 12.1 Ma (Mulch, 2016). This interpretation still suggests and argues for little to no surface uplift over this time. While the interpretation in Mulch (2016) is updated from the Chamberlain and Poage (2000) interpretations, it still contradicts the uplift history of from other lines of geologic evidence for the southern Sierra Nevada.

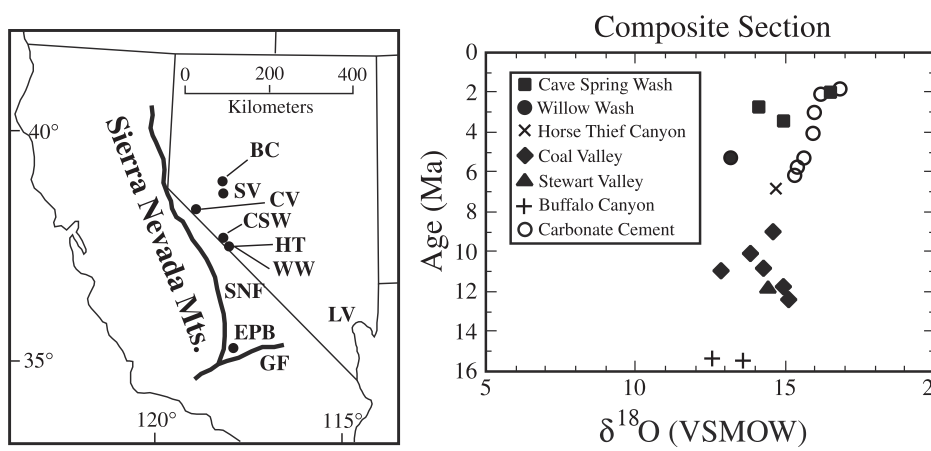

Figure 1.5. Location map and composite of smectite formed from the weathering of volcanic ash and carbonate cements collected on the leeside of the southern Sierra Nevada. Location map for sampled sections in the western Basin and Range. Abbreviations are as follows: BC, Buffalo Canyon; SV, Stewart Valley; CV, Coal Valley; CSW, Cave Spring Wash; WW, Willow Wash; HT, Horse Thief Canyon; EPB, El Paso Basin; LV, Las Vegas; SNF, Sierra Nevada Fault; GF, Garlock fault. Figure from Poage and Chamberlain (2002). The lack of change in the $\delta^{18}O$ of the samples collected suggests that there has been little to no uplift of the Sierra Nevada over the last 16 Ma.

1.3. Atmosphere-mountain interactions and the isotopic composition of precipitation

While it seems that modern isotopes are related to the elevation of a mountain range, interpreting paleo-records of the isotopic composition of precipitation in a mountain range in order to estimate the uplift history may be more difficult than initially thought. As more and more studies of isotope-based paleoaltimetry began to contradict other lines of geologic evidence, the underlying assumptions within the technique have been called into question (e.g. Galewsky, 2009a; Galewsky, 2009b; Lechler and Galewsky, 2013; Molnar, 2010; Wakabayashi, 2013). Are the geologic materials being sampled truly retaining a record of past meteoritic isotopes or have they been altered in some way? Can the changes in δ-values definitively be attributed to changes in elevation rather than changes in climate? Do windward lapse rates change with large-scale changes in climate or changes in elevation? How do atmospheric flow patterns impact the δ-values of precipitation? Is pure upslope flow an appropriate model of atmospheric dynamics for understanding and interpreting isotope-based paleoaltimetry? Several studies have been devoted to addressing each of these questions and this dissertation aims to address those that are related to atmospheric flow around mountain ranges.

Isotope-based paleoaltimetry interpretations rely on some combination of simple assumptions about atmospheric dynamics. Some of these common assumptions include:

purely 2-D flow over topography (e.g. Poage and Chamberlain, 2001); air masses do not mix (e.g. Rowley et al., 2001); or that the isotopic lapse rate does not change significantly with changes in elevation or climate (e.g. Cassel et al., 2009). In a 2-D model of pure orographic precipitation, the incoming air is lifted, cooled, and the heavier isotopes are preferentially condensed and rained out along the windward path. Subsidence in the lee may then suppress further precipitation downstream. In reality, atmosphere-mountain interactions are more complex. First, atmospheric flow patterns may not be defined by 2-D flow patterns (e.g. Friedman et al., 2002; Lechler and Galewsky, 2013) and second, pure orographic precipitation is rare, and few mountain ranges are dominated by simple upslope flow. More typically, precipitation is orographically enhanced within a larger scale weather system (e.g. Houze, 2012; Galewsky and Sobel, 2005). Changes in climate and atmospheric circulation can lead to a more complicated relationship between isotopic composition of precipitation and elevation (Molnar, 2010; Galewsky, 2009b; Insel et al., 2012; Wheeler et al., 2016). Some paleoaltimetry studies do recognize some of the limitations to interpreting paleoelevation and have tried to incorporate more complex atmospheric dynamics into their interpretations (e.g. Mulch, 2016; Winnick et al., 2014; Rowley, 2007).

Until recently, one of the major, if implicit, assumptions in leeside isotope-based paleoaltimetry models is that atmospheric flow around and a mountain range is 2-D, implying that leeside isotope records come from air masses that have traveled W-E and surmounted the range crest (e.g. Chamberlain and Poage, 2000). The stable isotope composition of waters in the Great Basin is not consistent with 2-D atmospheric flow over the southern Sierra Nevada, however. Most of the precipitation that reaches the eastern Great Basin is deflected to the north or south of the range (Friedman et al., 2002). Modern trajectory analyses for locations on the leeside of the Sierra Nevada find that flow is diverted around, rather than over, the highest topography (Lechler and Galewsky, 2013). This is especially true in the southern Sierra Nevada, where deflection dominates the flow path for areas above 2.5 km. This begs the question, if atmospheric flow is not 2-D, are isotope records able to constrain the timing and magnitude of surface uplift?

Recently there has been a push to investigate the relationship between the isotopic composition of precipitation and elevation using numerical models. General Circulation Models (GCMs) of modern and paleoclimates and idealized models of atmospheric flow over simplified ridges have shed light on the controls of this relationship, and the implications that has for isotope-based paleoaltimetry estimates. Several studies using GCMs with varying degrees of isotope-enabled tracing or microphysics schemes have been used to interpret paleoaltimetry isotope records (e.g. Poulsen et al., 2007; Insel et al., 2012; Feng et al., 2016; Herold et al., 2014). Each of these studies used GCMs to address some aspect of the change in isotopic composition of precipitation due to changes in elevation, climate, or land surface vegetation. Idealized models of atmospheric flow seek to systematically control atmospheric conditions and topography to determine how changes in elevation and climate affect the isotopic composition of precipitation. Both 2-D and 3-D simulations, with (e.g. Galewsky, 2009a; Moore et al., 2016) and without (e.g. Galewsky, 2008; Wheeler et al., 2016) isotope microphysics have investigated this relationship and found that changes in ridge height and climate can affect the windward and leeside isotopic composition of precipitation. Specifically, changes in ridge height and climate lead to changes in flow deflection around a ridge and that along the windward side, lapse rates for models of simple upslope flow diverge from Rayleigh distillation models (Galewsky, 2009).

Atmospheric flow over topography can be understood, to first order, in terms of the nondimensional flow parameter *Nh/U*; where *N* is the Brunt-Väisälä frequency (s^{-1}), *h* is the mountain height (m), and *U* is the horizontal wind speed (m/s) (e.g. Epifanio and Durran, 2001). Idealized models of atmospheric flow around topographic barriers suggest that when *Nh/U* << 1, flow tends to pass over the topographic barrier, but when *Nh/U* >> 1, flow tends to be deflected around the topographic barrier (Figure 1.6) (Galewsky, 2009).

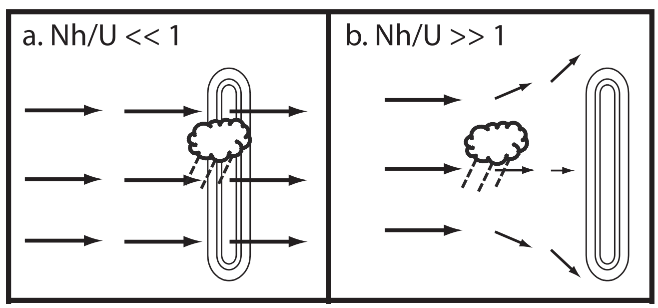

Figure 1.6. Schematic illustrating the relationship between the nondimensional flow parameter, *Nh/U* and flow over (a) and around (b) 3-D topography. Map view of flow. Figure from Galewsky (2009b).

Using numerical models of idealized flow, GCMs, and modern climate data this dissertation investigates some of the underlying assumptions implicit in both leeside and windward isotope-based paleoaltimetry studies. Through the framework of *Nh/U*, Chapters 2 and 4 focus on the impact of atmospheric flow patterns on leeside isotope-based paleoaltimetry reconstructions in the southern Sierra Nevada and the Southern Alps. Chapter 3 focuses on windward isotope-based paleoaltimetry through simulations of orographically enhanced precipitation. Specifically, how lapse rates change with increasing elevation and whether Rayleigh distillation models sufficiently reproduce simulated lapse rates.

1.4 References for Chapter 1

Abbott, L.D., Silver, E.A., Anderson, R.S., Smith, R., Ingle, J.C., Kling, S.A., Haig, D., Small, E., Galewsky, J., and Sliter, W., 1996, Measurement of tectonic surface uplift rate in a young collisional mountain belt: Nature, v. 385, p. 501–507.

Batt, G.E., Braun, J., Kohn, B.P., and McDougall, I., 2000, Thermochronological analysis of the dynamics of the Southern Alps , New Zealand: GSA Bulletin, v. 112, p. 250–266.

Cassel, E.J., Graham, S. a., and Chamberlain, C.P., 2009, Cenozoic tectonic and topographic evolution of the northern Sierra Nevada, California, through stable isotope paleoaltimetry in volcanic glass: Geology, v. 37, p. 547–550, doi: 10.1130/G25572A.1.

Chamberlain, C.P., and Poage, M.A., 2000, Reconstructing the paleotopography of mountain belts from the isotopic composition of authigenic minerals: , p. 115–118.

Chamberlain, C.P., Poage, M.A., Craw, D., and Reynolds, R.C., 1999, Topographic development of the Southern Alps recorded by the isotopic composition of authigenic clay minerals, South Island, New Zealand: Chemical Geology, v. 155, p. 279–294, doi: 10.1016/S0009-2541(98)00165-X.

Clark, M.K., Maheo, G., Saleeby, J., and Farley, K.A., 2005, The non-equilibrium landscape of the southern Sierra Nevada, California: GSA Today, v. 5173, p. 4–10.

Dansgard, W., 1964, Stable isotopes in precipitation: Tellus, v. 16, p. 436–468.

Ducea, M.N., and Saleeby, J.B., 1996, Buoyancy sources for a large, unrooted mountain range, the Sierra Nevada, California: Evidence from xenolith thermobarometry: v. 101, p. 8229–8244.

England, P., and Molnar, P., 1990, Surface uplift, uplift of rocks, and exhumation of rocks: Geology, v. 18, p. 1173–1177.

Epifanio, C.C., and Durran, D.R., 2001, Three-Dimensional Effects in High-Drag-State Flows over Long Ridges: Journal of the Atmospheric Sciences, v. 58, p. 1051–1065, doi: 10.1175/1520-0469(2001)058<1051:TDEIHD>2.0.CO;2.

Feng, R., Poulsen, C.J., and Werner, M., 2016, Tropical circulation intensification and tectonic extension recorded by Neogene terrestrial δ18O records of the western

United States: Geology, v. 44, p. 971–974, doi: 10.1130/G38212.1.

Friedman, I., Harris, J.M., Smith, G.I., and Johnson, C.A., 2002, Stable isotope composition of waters in the Great Basin, United States 1. Air-mass trajectories: Journal of Geophysical Research: Atmospheres, v. 107, doi: 10.1029/2001JD000565.

Galewsky, J., 2008, Orographic Clouds in Terrain-Blocked Flows: An Idealized Modeling Study: Journal of the Atmospheric Sciences, v. 65, p. 3460–3478, doi: 10.1175/2008JAS2435.1.

Galewsky, J., 2009a, Orographic precipitation isotopic ratios in stratified atmospheric flows: Implications for paleoelevation studies: Geology, v. 37, p. 791–794, doi: 10.1130/G30008A.1.

Galewsky, J., 2009b, Rain shadow development during the growth of mountain ranges: An atmospheric dynamics perspective: Journal of Geophysical Research: Earth Surface, v. 114, doi: 10.1029/2008JF001085.

Galewsky, J., and Sobel, A., 2005, Moist Dynamics and Orographic Precipitation in Northern and Central California during the New Year's Flood of 1997: Monthly Weather Review, v. 133, p. 1594–1612, doi: 10.1175/MWR2943.1.

Garzione, C.N., Hoke, G.D., Libarkin, J.C., Withers, S., MacFadden, B., Eiler, J., Ghosh, P., and Mulch, A., 2008, Rise of the Andes: Science, v. 320, p. 1304–1307, doi: 10.1126/science.1148615.

Garzione, C.N., Quade, J., DeCelles, P.G., and English, N.B., 2000, Predicting paleoelevation of Tibet and the Himalaya from d18O versus altitude gradients in meteoric water across the Nepal Himalaya: Earth and Planetary Science Letters, v. 183, p. 215–229.

Ghosh, P., Garzione, C.N., and Eiler, J.M., 2006, Rapid Uplift of the Altiplano Revealed through 13C-18O Bonds in Paleosol Carbonates: Science, v. 311, p. 511–515.

Herold, N., Buzan, J., Seton, M., Goldner, A., Green, J.A.M., Müller, R.D., Markwick, P., and Huber, M., 2014, A suite of early Eocene (~ 55 Ma) climate model boundary conditions: Geoscientific Model Development, v. 7, p. 2077–2090, doi: 10.5194/gmd-7-2077-2014.

Houze, R.A., 2012, Orographic Effects on Precipitating Clouds: , p. 1–47, doi: 10.1029/2011RG000365.1.INTRODUCTION.

Hren, M.T., Pagani, M., Erwin, D.M., and Brandon, M., 2010, Biomarker reconstruction of the early Eocene paleotopography and paleoclimate of the northern Sierra Nevada: Geology, v. 38, p. 7–10, doi: 10.1130/G30215.1.

Ingraham, N.L., and Taylor, B.E., 1991, Light Stable Isotope Systematics of Large-Scale Hydrologic Regimes in California and Nevada: Water Resources Research, v. 27, p. 77–90.

Insel, N., Poulsen, C.J., Ehlers, T.A., and Sturm, C., 2012, Response of meteoric δ18O to surface uplift: Implications for Cenozoic Andean Plateau growth: Earth and Planetary Science Letters, v. 317–318, p. 262–272, doi: 10.1016/j.epsl.2011.11.039.

Lechler, A.R., and Galewsky, J., 2013, Refining paleoaltimetry reconstructions of the Sierra Nevada: California, using air parcel trajectories: Geology, v. 41, p. 259–262, doi: 10.1130/G33553.1.

Mahéo, G., Saleeby, J., Saleeby, Z., and Farley, K.A., 2009, Tectonic control on southern Sierra Nevada topography, California: Tectonics, v. 28, doi: 10.1029/2008TC002340.

Merritts, D., and Ellis, M., 1994, Introduction to special section on tectonics and topography and topography: Journal of Geophysical Research, v. 99, p. 12,135-12,141.

Molnar, P., 2010, Deuterium and oxygen isotopes, paleoelevations of the Sierra Nevada, and Cenozoic climate: Bulletin of the Geological Society of America, v. 122, p. 1106–1115, doi: 10.1130/B30001.1.

Molnar, P., and H. Lyon-Caen, 1988, Some simple physical aspects of the support, structure, and evolution of mountain belts, Geological Society of America Special Paper, v. 218, p. 179-207.

Moore, M., Blossey, P.N., Muhlbauer, A., and Kuang, Z., 2016, Microphysical controls on the isotopic composition of wintertime orographic precipitation: Journal of Geophysical Research: Atmospheres, v. 121, p. 7235–7253, doi: 10.1002/2015JD023763.The.

Mulch, A., 2016, Stable isotope paleoaltimetry and the evolution of landscapes and life: Earth and Planetary Science Letters, v. 433, p. 180–191, doi: 10.1016/j.epsl.2015.10.034.

Mulch, A., Graham, S.A., and Chamberlain, C.P., 2006, Hydrogen Isotopes in Eocene River Gravels and Paleoelevation of the Sierra Nevada: v. 313, p. 87–89.

Mulch, A., Sarna-Wojcicki, A.M., Perkins, M.E., and Chamberlain, C.P., 2008, A Miocene to Pleistocene climate and elevation record of the Sierra Nevada (California): Proceedings of the National Academy of Sciences of the United States of America, v. 105, p. 6819–6824, doi: 10.1073/pnas.0708811105.

Poage, M.A., and Chamberlain, C.P., 2001, Empirical relationships between elevation and the stable isotope composition of precipitation and surface waters: considerations for studies of paleoelevation change: American Journal of Science: v. 301, p. 1–15.

Poage, M.A., and Chamberlain, C.P., 2002, Stable isotopic evidence for a Pre-Middle Miocene rain shadow in the western Basin and Range: Implications for the paleotopography of the Sierra Nevada: Tectonics, v. 21, doi: 10.1029/2001TC001303.

Poulsen, C.J., Sciences, G., Arbor, A., and Pollard, D., 2007, General circulation model simulation of the δ18O content of continental precipitation in the middle Cretaceous: A model-proxy comparison: Geology, v. 36, no. 3, p. 199–202, doi: 10.1130/G23343A.1.

Rowley, D.B., 2007, Stable Isotope-Based Paleoaltimetry: Theory and Validation: Reviews in Mineralogy and Geochemistry, v. 66, p. 23–52, doi: 10.2138/rmg.2007.66.2.

Rowley, D.B., Pierrehumbert, R.T., and Currie, B.S., 2001, A new approach to stable isotope-based paleoaltimetry: Implications for paleoaltimetry and paleohypsometry of the High Himalaya since the late Miocene: Earth and Planetary Science Letters, v. 188, p. 253–268, doi: 10.1016/S0012-821X(01)00324-7.

Sutherland, R., 1995, The Australia-Pacific boundary and Cenozoic plate motions in the SW Pacific: Some constraints from Geosat data: v. 14, p. 819–831.

Taylor, H.P., 1974, The Application of Oxygen and Hydrogen Isotope Studies to Problems of Hydrothermal Alteration and Ore Deposition: Economic Geology, v. 69, p. 843–883.

Wakabayashi, J., 2013, Paleochannels, stream incision, erosion, topographic evolution, and alternative explanations of paleoaltimetry, Sierra Nevada, California: Geosphere, v. 9, p. 191–215, doi: 10.1130/GES00814.1.

Walcott, R.I., 1998, Modes of Oblique Compression: Late Cenozoic Tectonics of the Souther Island of New Zealand: Reviews of Geophysics, v. 36.

Wheeler, L.B., Galewsky, J., Herold, N., and Huber, M., 2016, Late Cenozoic surface uplift of the southern Sierra Nevada (California, USA): A paleoclimate perspective on lee-side stable isotope paleoaltimetry: Geology, v. 44, no.6, p. 451–454, doi: 10.1130/G37718.1.

Winnick, M.J., Chamberlain, C.P., Caves, J.K., and Welker, J.M., 2014, Quantifying the Isotopic “Continental Effect”: Earth and Planetary Science Letters, v. 406, p. 123–

133, doi: 10.1016/j.epsl.2014.09.005.

Winograd, I.J., Szabo, B.J., Coplen, T.B., Riggs, A.C., and Kolesar, P.T., 1985, Two-Million-Year Record of Deuterium Depletion in Great Basin Ground Waters: Science, v. 227, p. 519–522.

2. LATE CENOZOIC SURFACE UPLIFT OF THE SOUTHERN SIERRA NEVADA: A PALEOCLIMATE PERSPECTIVE ON LEESIDE STABLE ISOTOPE PALEOALTIMETRY

2.1. Abstract

Proposed estimates of Late Cenozoic surface uplift in the Southern Sierra Nevada (Sierra) range anywhere from 0 to 2 km. Recent interpretations of leeside isotope records from the southern Sierra suggest that the elevation of the southern Sierra has been sufficiently high to induce similar-to-modern atmospheric flow patterns since ~12 Ma. We test the sensitivity of flow deflection to elevation to determine what elevation is sufficiently high to establish modern flow patterns. The tendency for flow to deflect around a topographic barrier can be determined by the atmospheric stability, barrier height, and incoming wind speed. Utilizing global paleoclimate models and idealized regional weather models, we find that the Miocene atmosphere was more stable than modern. We suggest that in a Miocene climate, similar-to-modern flow patterns could have been achieved for elevations as low as 2 km and that while Miocene leeside isotope records from the southern Sierra may indicate that the southern Sierra have been a longstanding topographic feature, they may be unable to resolve the proposed Late Cenozoic surface uplift of the southern Sierra.

2.2. Introduction

Several lines of evidence suggest that the southern Sierra Nevada (Sierra) have experienced 1-2 km of surface uplift over the last 20 Ma (Wakabayashi, 2013 and references therein). Interpretations of leeside stable isotope-based paleoaltimetry studies suggest that the southern Sierra were high enough to induce similar-to-modern atmospheric flow trajectories since ~12 Ma (Mulch, 2016), but the elevation required to support modern flow trajectories is poorly known, and the extent to which leeside proxies can constrain Late Cenozoic surface uplift of the southern Sierra is still debated. Lechler and Galewsky (2013) showed that air parcel trajectories tend to travel around the highest part of the southern Sierran topography, but they focused exclusively on the modern climate, leaving open the key question of whether or not modern flow deflection observed in the southern Sierra persisted through past climates. If past climates supported significantly less flow deflection than we see today, then leeside isotope-based proxy records may have had the potential to faithfully record changes in the elevation of the southern Sierra associated with the proposed Late Cenozoic surface uplift. The goal of this study is to explore the extent to which paleoclimate may have influenced flow deflection and leeside isotope-based paleoaltimetry proxies in the southern Sierra during the Late Cenozoic, a key period for understanding the surface uplift history of the Sierra.

2.3. Background

2.3.1. Miocene tectonics of the southern Sierra

The tectonic evolution of the northern and southern Sierra are topics of considerable debate, and their surface uplift histories are thought to be significantly different from each another (e.g. Chamberlain et al., 2012; Wakabayashi, 2013; Gabet, 2014; and Mulch, 2016; and references therein). In this paper we focus exclusively on the southern Sierra, south of the Stanislaus river and north of the Kern river (Figure 2.1).

Clark et al. (2005) and Wakabayashi (2013) proposed two pulses of surface uplift in the southern Sierra over the last 20 Ma. The first pulse may have been driven by the opening of a slab window during the northward migration of the Mendocino triple junction (Wakabayshi, 2013). The event began in the Kern to Kings River drainages ~20 Ma, migrated north through the San Joaquin River drainage between 10-6 Ma, and the Mokelumne and Stanislaus River drainages around 4–3.6 Ma (Mahéo et al., 2009). The second pulse was relatively synchronous between the southern Sierra river basins and may have been driven by the delamination of high-density material beneath the southern Sierra post-3.6 Ma (Ducea and Saleeby, 1996).

Early interpretations of leeside isotope records for the southern Sierra suggested that the stability of precipitation δ-values over time indicated that there may have been relatively little surface uplift since ~18 Ma (Poage and Chamberlain, 2002; Crowley et al., 2008). More recent interpretations highlight some of the limitations of the technique (e.g. Mulch, 2016; Chamberlain et al., 2012) and suggest that the southern Sierra may have been sufficiently high to induce similar-to-modern flow patterns since ~12 Ma (Mulch, 2016). We address the question of how high is sufficiently high to induce similar-to-modern flow patterns in the southern Sierra and the implications this has for understanding the evolution of the southern Sierra in the Late Cenozoic.

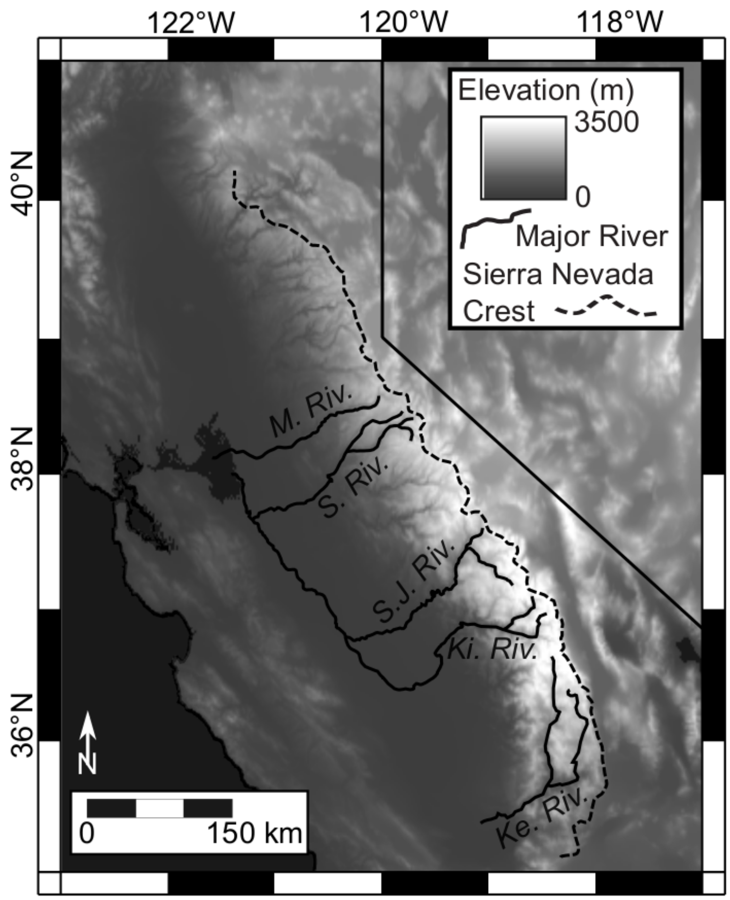

Figure 2.1. Topography of the Sierra Nevada. The Late Cenozoic surface uplift of the southern Sierra is focused on the region to the south of the San Joaquin river and to the north of the Kern river. The solid lines are major rivers: 1 – Mokelumne; 2. – Stanislaus; 3 – San Joaquin; 4 – Kings; 5 – Kern. The dashed line is the Sierra range crest. The stars mark the location of $\delta^{18}O$ sampling locations for the southern Sierra from Poage and Chamberlain (2002). The enclosed dashed line marks the region where the low δD values in 17 volcanic glass samples from Mulch (2008) are interpreted as indicating the establishment of similar-to-modern flow deflection since ~12 Ma (Mulch, 2016).

2.3.2. Modern Flow Deflection in the Southern Sierra

Until recently, one of the major, if implicit, assumptions in leeside isotope-based paleoaltimetry models is that atmospheric flow around and a mountain range is 2-D, implying that leeside isotope records come from air masses that have traveled W-E and surmounted the range crest. As an air mass is lifted along the windward side, water vapor condenses, and the heavier isotopes are preferentially rained out. With increasing elevation and as the air mass reaches the leeside, d-values are increasingly more negative. The magnitude of change in the isotopes across the range crest into the leeside is thought to record the maximum elevation along that path (Chamberlain and Poage, 2000). The stable isotope composition of waters in the Great Basin is not consistent with 2-D atmospheric flow over the southern Sierra, however. Most of the precipitation that reaches the eastern Great Basin was deflected to the north or south of the range (Friedman et al., 2002). Modern trajectory analyses for locations on the leeside of the Sierra find that flow is diverted around, rather than over, the highest topography (Lechler and Galewsky, 2013). This is especially true in the southern Sierra, where deflection dominates the flow path for areas above 2.5 km.

Atmospheric flow over topography can be understood, to first order, in terms of the nondimensional flow parameter *Nh/U*; where *N* is the Brunt-Väisälä frequency (s^{-1}), *h* is the mountain height (m), and *U* is the horizontal wind speed (m/s) (e.g., Epifanio and Durran, 2001). Idealized models of atmospheric flow around topographic barriers suggest that when $Nh/U \ll 1$, flow tends to pass over the topographic barrier, but when $Nh/U \gg 1$, flow tends to be deflected around the topographic barrier (Galewsky, 2009). In order for leeside proxies in the southern Sierra to have quantitatively recorded the highest elevations, *Nh/U* during the Miocene needed to be lower than modern. This is the issue we address in this paper.

2.4. Methods

2.4.1. Atmospheric Stability of the Sierra

To determine how changes in climate influence flow deflection in the Sierra, we calculated the annual and storm average upstream flow parameters for simulations of a Pre-Industrial (PI) and a Miocene climate. The simulations were run using the Community Earth System Model (CESM) v1.0.5 (Gent et al., 2011). The atmospheric component of our simulations were configured with a ~2 × 2 degree horizontal resolution and 26 vertical levels. The PI simulation was run with boundary conditions representing the year 1850. The Miocene simulation was forced with vegetation, topography, and CO_2 representing 20–14 Ma, and was run for over 2,000 years to ensure equilibrium. The Miocene simulation was updated from Herold et al. (2011) and more can be found in Chapter 6 in the Supplemental Materials.

The upstream flow parameter calculations apply to both the northern and southern Sierra. We establish a windward and leeward region for both the PI and Miocene Sierra. The windward region is the area to the east of the coastline and the west of the range crest for the length of the Sierra. The leeward region is the area between the range crest and two degrees east for the length of the Sierra. The upstream flow parameters are regional averages from the windward region. Due to the coarse resolution of the CESM simulations we do not calculate the Brunt-Väisälä frequency; instead, we calculate the static stability, a measure of the change in temperature with height and determines the Brunt-Väisälä frequency (Frierson, 2006). The moist static stability (q_{ez}) is the difference between the saturated equivalent potential temperature at 400 hPa and the equivalent potential temperature at the surface. The dry static stability (q_z) is the difference between the potential temperature at 400 hPa and the potential temperature at the surface (Frierson, 2006). U is an average of the wind speeds between 500 hPa and the surface. Since leeside isotope records are generated during leeside precipitation, we calculate storm averages for q_{ez}, q_z, and U. A storm was selected if there was precipitation in both the leeward and windward region.

2.4.2. Simulations of Flow around Idealized Terrain

Using the Weather Research and Forecasting (WRF) model V3.5.1 (Skamarock et al., 2008) we ran idealized simulations to determine the climate conditions required for the 2-D assumptions used in the leeside proxies to faithfully record the elevation in two idealized topographic scenarios: (1) a uniform ridge 2.5 km high ('Low Southern Sierra') and (2) a 2.5 km high ridge with a southern region 4 km high ('High Southern Sierra'). These are idealized scenarios to develop our intuition about flow over Sierran-scale topography and do not necessarily embody any particular theory for the geological evolution of the Sierra. The model domain is 564 × 250 points with 4 km horizontal grid spacing and 121 unevenly spaced vertical levels extending to 30 km.

First, we tested the sensitivity of flow deflection to the High Southern Sierra model to changes in the atmospheric conditions during a storm-like event. The High Southern Sierra model topography is based on the modern configuration of the Sierra, and is a 500 km long by 80 km wide ridge (Figure 2.2A). The atmospheric conditions are set by the moist Brunt-Väisälä frequency (N_m). We used a constant U for all simulations, the average incoming storm wind profile from the PI and Miocene. Surface winds were set at 5 m/s, increasing to 30 m/s at the tropopause (~11 km), and decreasing to 10 m/s at the model top (Figure 2.2B). Initial conditions are after Galewsky (2008). Each simulation has an initial relative humidity of 98% and surface temperature of 16 °C. Above the tropopause we use a dry Brunt-Väisälä frequency (N_d) of 0.02 s^{-1}.

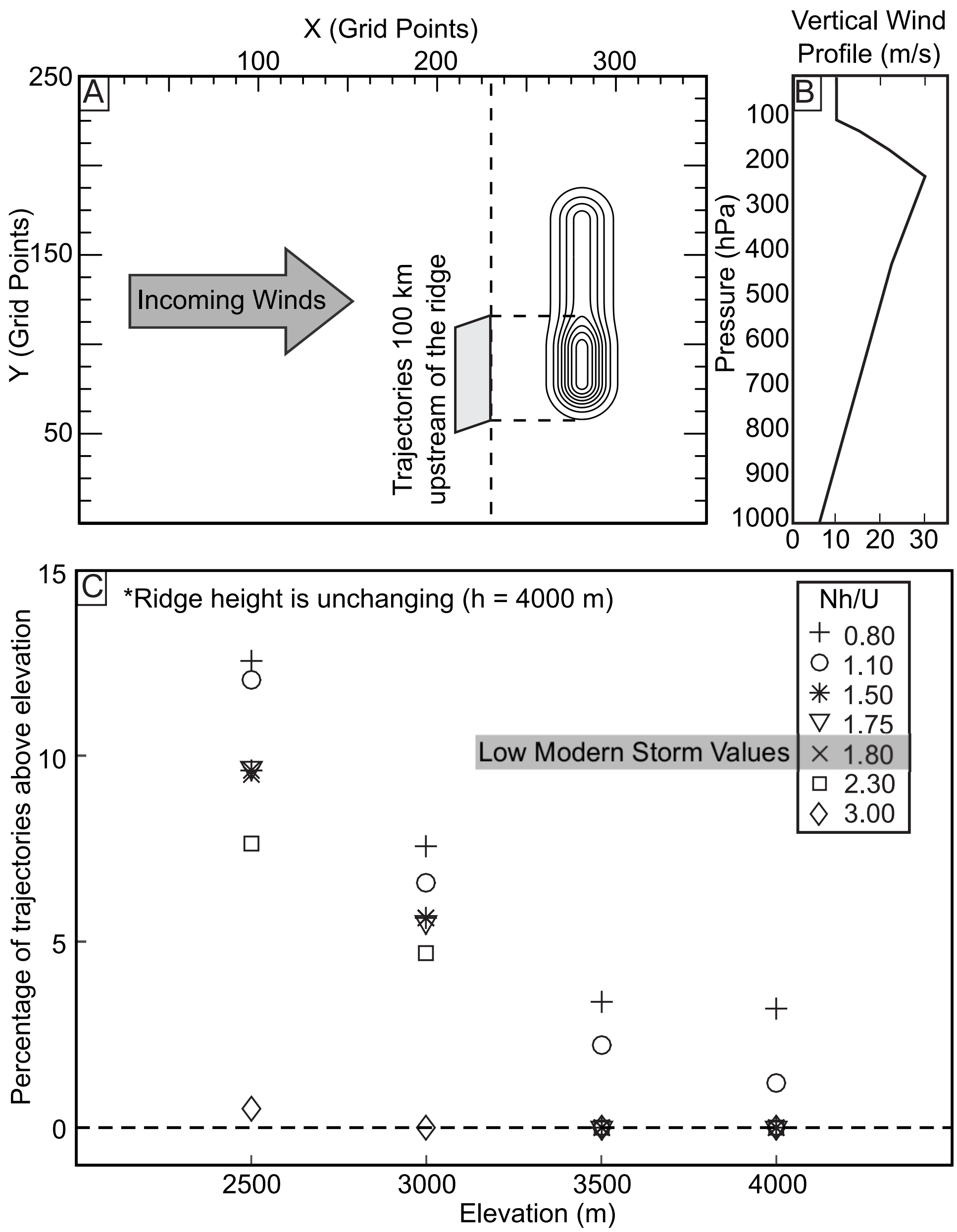

Figure 2.2. A: Model domain and the idealized terrain. Topographic setup for the High Southern Sierra model, the high ridge is 4 km and the low ridge is 2.5 km, contour intervals are 500 m. The gray region is the initial trajectory positions; the arrow indicates the direction of the incoming winds. B: Initial vertical wind conditions. C: Points indicate the percentage of trajectories that pass over the threshold elevation for the idealized high Sierra. Low values of modern *Nh/U* calculated from NARR in gray. Note that the *y*-axis only extends to 15%.

To test the sensitivity of flow deflection to elevation and the Low Southern Sierra model we ran simulations of flow deflection around a uniform ridge, ranging in elevation from 1 to 3.5 km, under a less stable climate. We used a low value of N_m to quantify flow deflection for low values of *Nh/U*. The ridge length, width, and the initial atmospheric conditions are the same as in previous simulations.

To quantify flow deflection, we ran a forward trajectory analysis using Read/Interpolate/Plot version 4.6 (www2.mmm.ucar.edu/mm5/WRF_post/RIP4.htm). The trajectories started 100 km upstream of the ridge and extend from the model surface to 2 km in elevation with 100 m vertical and 4 km horizontal grid spacing. We selected 2 km to capture air masses that travel up the windward face of the topographic barrier.

2.5. Results

2.5.1. PI and Miocene Atmospheric Stability

Our first goal was to determine whether the climate during the Miocene was sufficiently different from modern and whether that climate supported 2-D or 3-D atmospheric flow in the southern Sierra. We calculated the annual and storm average upstream flow parameters for the Sierra for both the PI and Miocene simulated climates. For the PI simulation the annual average q_{ez} = 28 K and q_z = 23 K. The annual average U = 5.6 m/s. For the Miocene simulation the annual average q_{ez} = 48 K and q_z = 29 K. The annual average $U = 5.4$ m/s. For the PI simulation the storm average $q_{ez} = 32$ K and $q_z = 26$ K. The storm average $U = 9.2$ m/s. For the Miocene simulation the storm average $q_{ez} = 46$ K and $q_z = 31$ K. The Miocene storm average $U = 8.2$ m/s. Both Miocene q_{ez} and q_z were higher than the PI, meaning the Miocene Sierran climate was more stable than modern. From relative values of *Nh/U* for the Miocene and PI climates, assuming a high southern Sierra, *Nh/U* would have been greater during the Miocene. Thus, to first order, the Miocene climate as simulated here was even more stable than modern climate and would have supported even greater flow deflection around a modern southern Sierra topographic configuration. Although the Miocene simulation is forced with climate conditions for 20–14 Ma, there is no evidence to suggest that the last 14 Ma it was significantly less stable than modern.

2.5.2. Simulations of Flow Deflection

Although our results suggest that Miocene climate was more stable than modern, there is still a question of whether or not a less stable climate would support 2-D flow in the southern Sierra. Here, we quantify the degree of flow deflection around the High Southern Sierra model for a range of stabilities. As the threshold elevation and *Nh/U* increase, the percentage of trajectories that surmount the high ridge decreases (Figure 2.2C). When $Nh/U > 1.1$, none of the trajectories surmount the 4 km ridge crest. When $Nh/U < 1.1$, < 5% of trajectories surmount the 4 km ridge crest. For a threshold elevation of 2.5 km, very few of the trajectories surmount the highest elevations of the ridge crest, <15% of trajectories surmount 2.5 km when $Nh/U > 1.1$.

We also tested the sensitivity of flow deflection to changes in elevation. For simulations of flow around a uniform ridge, as elevation increases, the percent of trajectories surmounting the ridge crest decreases (Figure 2.3). For a ridge with a maximum elevation of 2.5 km, <50% of trajectories surmount the ridge crest. For a 2 km ridge where $N_m = 0.0075\ s^{-1}$, near low modern storm values (see Chapter 6 Supplemental Materials), 42% of trajectories surmount the 2 km ridge crest. For a low ridge under modern conditions, >50% of atmospheric flow would be deflected around the mountain range, suggesting that modern patterns of flow deflection could have been established for a before Late Cenozoic uplift of the southern Sierra.

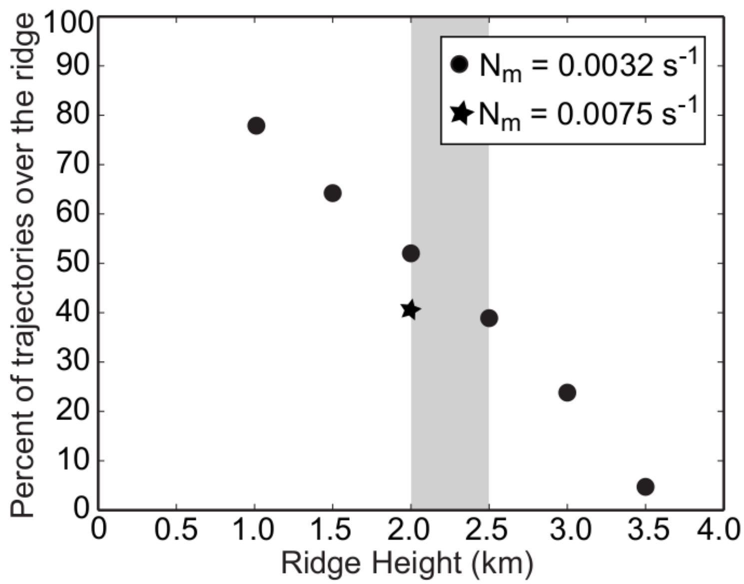

Figure 2.3. Percent of trajectories that surmount the ridge crest for a uniform ridge of different elevations. N_m and U are the same for all simulations. Early Miocene southern Sierra elevation estimates that assume late Cenozoic uplift are shaded in gray.

2.6. Discussion

Our results are summarized in Figure 2.4, which outlines the two idealized topographic models of the southern Sierra and the changes in atmospheric flow under modern and Miocene climates. Figure 2.4A and 2.4B represent the modern Sierra in a modern climate. Under modern conditions, *Nh/U* is high and atmospheric flow is deflected around the high southern Sierra (Lechler and Galewsky, 2013; Friedman et al., 2002). Under modern conditions we would not expect air masses to surmount the southern crest or for the leeside precipitation isotopic composition to record the elevation of the southern Sierra. Instead, air masses travel up the windward face to 2 to 2.5 km, and deflect around the southern crest before reaching the leeside, recording the degree of flow deflection. In order for leeside isotope proxies to quantify the extent of Late Cenozoic uplift, incoming air masses must travel perpendicular to the range and over the southern crest before reaching the leeside. Therefore, Miocene *Nh/U* needed to have been significantly lower than modern. This was not the case. Figure 2.4C shows the high southern Sierra model in a Miocene climate. Flow deflection around the southern Sierra is greater than in Figure 2.4A since *Nh/U* during the Miocene was greater than modern. Figure 2.4D shows atmospheric deflection for the Low Southern Sierra model in a Miocene climate. Under modern atmospheric conditions for a 2 to 2.5 km ridge, >50% of flow is blocked. The simulated atmospheric stability during the Miocene was greater than modern, meaning that flow deflection for a 2 to 2.5 km ridge during the Miocene would have been greater. If the southern Sierra were 2 to 2.5 km during the Miocene, deflection may have already dominated the flow path.

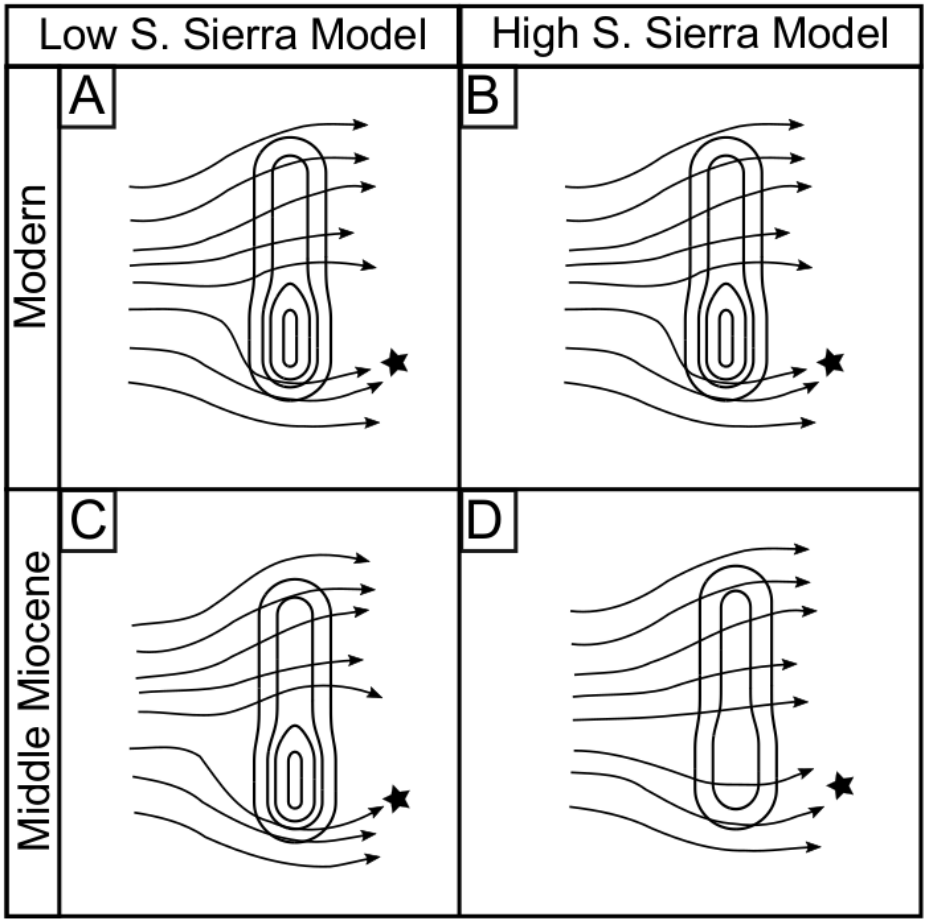

Figure 2.4. Summary of atmospheric flow deflection for the High and Low Southern Sierra models. Contours are for a simplified Sierra topography at 1 km intervals. The star marks an example location for leeside proxies. Conditions for both the High (A) and Low (B) Southern Sierra models in the modern are the same, atmospheric flow deflection dominates the flow path to the leeside of the southern ridge. For the High Southern Sierra model (C) flow deflection would have been greater than modern. For the Low Southern Sierra model (D) flow deflection was likely >50% for a 2 to 2.5 km ridge. Due to the 3-D nature of flow during past and present climates that the leeside isotopes may not have been able to distinguish between these two models.

In a 2-D model of purely orographic precipitation, the incoming air is lifted and cooled, and the heavier isotopes are preferentially condensed and rained out along the windward path. Subsidence in the lee may then suppress further precipitation downstream. In this case, there may be no leeside record of elevation in meteoric waters.

Pure orographic precipitation is rare, however. More typically, precipitation in the Sierra is orographically enhanced within a larger-scale weather system (e.g., Galewsky and Sobel, 2005). If the storm traveled W-E and over the range crest, downstream d-values in the remaining water vapor may retain a signal of elevation, and would be more negative than if that same storm was deflected around the south of the range.

Although there are many reasons why orographic precipitation d-values may not strictly record the elevation of a range crest (e.g., Rohrmann et al., 2014; Insel et al., 2012), here we focused solely on the influence of flow deflection. *Nh/U* determines the tendency of an air mass to surmount a topographic barrier. When *Nh/U* is high, air masses tend to be deflected around the barrier and there is limited orographic influence on the isotopic composition. All other things being equal, precipitation from an air mass traveling perpendicular to the range front and deflected around the crest would have higher d-values than an air mass that traveled over the range crest to that same leeside location. If deflection around the range crest was the primary pathway through time, the d-values on the leeside might change relatively little with changes in elevation.

Mulch (2016) suggested that the southern Sierra were high enough to induce similar-to-modern air mass trajectories since ~12 Ma. Our results suggest that the modern pattern of flow deflection around the southern Sierra may be established when the southern Sierra exceeded an elevation of 2 to 2.5 km and that such conditions would have been the case since the Miocene. The proposed Late Cenozoic surface uplift of the Sierra Nevada is thought to have increased the elevation of the southern Sierra from 2-3 km to 4 km (Wakabayashi, 2013). Our results suggest that leeside proxy records would thus have been dominated by flow deflection even before such surface uplift occurred and may simply reflect the long-term presence of topography in the southern Sierra.

2.7. Conclusions

The goal of this paper was to determine the elevation at which similar-to-modern atmospheric flow patterns would have been established for the southern Sierra Nevada, and to explore the implications of that result for understanding the Late Cenozoic geodynamic evolution of the Sierra. Our results suggest that Miocene climate was even more stable than modern and that atmospheric flow deflection in the Miocene could have dominated flow patterns for elevations as low as 2 km. As a result, leeside isotope records for the southern Sierra may only indirectly record Late Cenozoic surface uplift due to the 3-D nature of flow in the southern Sierra. We conclude that similar-to-modern flow patterns in the southern Sierra could have been achieved for elevations as low as 2 km during the Miocene and that leeside isotope records may only indicate that the southern Sierra have been a longstanding topographic feature. We further conclude that there may be no conflict between leeside isotope records in the southern Sierra and the body of evidence in support of Late Cenozoic uplift of the southern part of the range.

2.8. References in Chapter 2

Chamberlain, C.P., and Poage, M.A., 2000, Reconstructing the paleotopography of mountain belts from the isotopic composition of authigenic minerals: Geology, v. 28, p. 115–118, doi:10.1130/0091-7613(2000)28<115:RTPOMB>2.0.CO;2.

Chamberlain, C.P., Mix, H.T., Mulch, A., Hren, M.T., Kent-corson, M.L., Davis, S.J., Horton, T.W., and Graham, S.A., 2012, The Cenozoic Climate and Topographic Evolution of the Western North American Cordillera: v. 312, p. 213–262, doi: 10.2475/02.2012.05.

Clark, M.K., Maheo, G., Saleeby, J., and Farley, K.A., 2005, The non-equilibrium landscape of the southern Sierra Nevada, California: GSA Today, v. 15, p. 4–10, doi:10.1130/1052-5173(2005)015[4:TNLOTS]2.0.CO;2.

Crowley, B.E., Koch, P.L., and Davis, E.B., 2008, Stable isotope constraints on the elevation history of the Sierra Nevada Mountains, California: Geological Society of America Bulletin, v. 120, p. 588–598, doi:10.1130/B26254.1.

Ducea, M.N., and Saleeby, J.B., 1996, Buoyancy sources for a large, unrooted mountain range, the Sierra Nevada, California: Evidence from xenolith thermobarometry: Journal of Geophysical Research, v. 101, p. 8229–8244, doi:10.1029/95JB03452.

Epifanio, C.C., and Durran, D.R., 2001, Three-Dimensional Effects in High-Drag-State Flows over Long Ridges: Journal of the Atmospheric Sciences, v. 58, p. 1051–1065, doi:10.1175/1520-0469(2001)058<1051:TDEIHD>2.0.CO;2.

Friedman, I., Harris, J.M., Smith, G.I., and Johnson, C.A., 2002, Stable isotope composition of waters in the Great Basin, United States 1. Air-mass trajectories: Journal of Geophysical Research: Atmospheres, v. 107, doi: 10.1029/2001JD000565.

Frierson, D.M.W., 2006, Robust increases in midlatitude static stability in simulations of global warming: Geophysical Research Letters, v. 33, p. L24816, doi:10.1029/2006GL027504.

Gabet, E.J., 2014, Late Cenozoic Uplift of the Sierra Nevada, California? A critical analysis of the geomorphic evidence: American Journal of Science, v. 314, p. 1224–1257, doi: 10.2475/08.2014.03.

Galewsky, J., 2008, Orographic Clouds in Terrain-Blocked Flows: An Idealized Modeling Study: Journal of the Atmospheric Sciences, v. 65, p. 3460–3478, doi:10.1175/2008JAS2435.1.

Galewsky, J., 2009, Rain shadow development during the growth of mountain ranges: An atmospheric dynamics perspective: Journal of Geophysical Research: Earth Surface, v. 114, F01018.

Galewsky, J., and Sobel, A., 2005, Moist Dynamics and Orographic Precipitation in Northern and Central California during the New Year's Flood of 1997: Monthly Weather Review, v. 133, p. 1594–1612, doi:10.1175/MWR2943.1.

Gent, P.R., Danabasoglu, G., Donner, L.J., Holland, M.M., Hunke, E.C., Jayne, S.R., Lawrence, D.M., Neale, R.B., Rasch, P.J., Vertenstein, M., Worley, P.H., Yang, Z.L., and Zhang, M., 2011, The Community Climate System Model version 4: Journal of Climate, v. 24, p. 4973–4991, doi: 10.1175/2011JCLI4083.1.

Herold, N., Huber, M., and Müller, R.D., 2011, Modeling the miocene climatic optimum. Part I: Land and Atmosphere: Journal of Climate, v. 24, p. 6353–6372, doi:10.1175/2011JCLI4035.1.

Insel, N., Poulsen, C.J., Ehlers, T.A., and Sturm, C., 2012, Response of meteoric d18O to surface uplift: Implications for Cenozoic Andean Plateau growth: Earth and Planetary Science Letters, v. 317–318, p. 262–272, doi:10.1016/j.epsl.2011.11.039.

Lechler, A.R., and Galewsky, J., 2013, Refining paleoaltimetry reconstructions of the Sierra Nevada: California, using air parcel trajectories: Geology, v. 41, p. 259–262, doi:10.1130/G33553.1.

Mahéo, G., Saleeby, J., Saleeby, Z., and Farley, K.A., 2009, Tectonic control on southern Sierra Nevada topography, California: Tectonics, v. 28, p. TC6006, doi:10.1029/2008TC002340.

Mulch, A., Sarna-Wojcicki, A.M., Perkins, M.E., and Chamberlain, C.P., 2008, A Miocene to Pleistocene climate and elevation record of the Sierra Nevada (California): Proceedings of the National Academy of Sciences of the United States of America, v. 105, p. 6819–6824, doi:10.1073/pnas.0708811105.

Mulch, A., 2016, Stable isotope paleoaltimetry and the evolution of landscapes and life: Earth and Planetary Science Letters, v. 433, p. 180–191, doi:10.1016/j.epsl.2015.10.034.

Poage, M.A., and Chamberlain, C.P., 2002, Stable isotopic evidence for a Pre-Middle Miocene rain shadow in the western Basin and Range: Implications for the paleotopography of the Sierra Nevada: Tectonics, v. 21, doi:10.1029/2001TC001303.

Rohrmann, A., Strecker, M.R., Bookhagen, B., Mulch, A., Sachse, D., Pingel, H., Alonso, R.N., Schildgen, T.F., and Montero, C., 2014, Can stable isotopes ride out the storms? The role of convection for water isotopes in models, records, and paleoaltimetry studies in the central Andes: Earth and Planetary Science Letters, v. 407, p. 187–195, doi:10.1016/j.epsl.2014.09.021.

Skamarock, W.C., Klemp, J.B., Dudhi, J., Gill, D.O., Barker, D.M., Duda, M.G., Huang, X.-Y., Wang, W., and Powers, J.G., 2008, A Description of the Advanced Research WRF Version 3: NCAR Technical Note, NCAR/TN-475+STR, p. 113.

Wakabayashi, J., 2013, Paleochannels, stream incision, erosion, topographic evolution, and alternative explanations of paleoaltimetry, Sierra Nevada, California: Geosphere, v. 9, p. 191–215, doi:10.1130/GES00814.1.

3. A COMPARISON OF 1-D RAYLEIGH DISTILLATION MODELS FOR PALEOALTIMETRY AND SIMULATED δD LAPSE RATES IN AN IDEALIZED WINTER-TIME STORM

3.1. Abstract

Using an isotope enabled microphysics scheme in the Weather Research and Forecasting (WRF) model, we test the sensitivity of $\delta D_{precipitation}$ in an idealized winter-time storm around a simplified ridge to changes in elevation and compare the results to Rayleigh distillation models for the same atmospheric conditions. We compare the $\delta D_{precipitation}$ lapse rates from the WRF simulations to the Rayleigh distillation models. Rayleigh distillation models generally have steeper lapse rates than the WRF simulations even though the average atmospheric conditions are the same. Due to the high precipitation efficiency of Rayleigh distillation models, Rayleigh distillation will always yield the steepest lapse rates for a given temperature structure and may, as a result, under-estimate paleoelevation and consequently over-estimate the amount of surface uplift when used to interpret the paleo-elevation of a mountain range. Rayleigh distillation may therefore be most appropriate for determining the minimum elevation and the maximum amount of uplift provided that paleo-climate conditions can be constrained.

3.2. Introduction

Understanding the factors that control the isotopic composition of orographically enhanced precipitation ($\delta^{18}O$ and δD) is fundamental to improved isotope-based paleoaltimetry estimates. As elevation increases along a mountain front, the precipitation δ-values are more negative (Dansgaard, 1964). Paleoaltimetry uses records of the isotopic composition of meteoric water, through time, across mountain ranges to reconstruct the elevation history of that mountain range (Poage and Chamberlain, 2001). Studies of isotope-based paleoaltimetry typically use either empirically- or theoretically-based methods to reconstruct paleo-elevation. The empirical approach relies on modern global observations of the isotopic composition of waters and elevation. From studies of precipitation, surface water, rivers, firn and snow, Poage and Chamberlain (2001) found that lapse rates were roughly consistent globally at -2.8 ‰/km for $\delta^{18}O$, although with wide scatter. The theoretical approach relies on 1-D thermodynamic models of Rayleigh distillation to determine the change in δ-values with elevation for a given temperature profile and mixing ratio as an air parcel ascends (Rowley, 2007). In the California Sierra Nevada, studies have relied on both of these methods to investigate the uplift history across a range of time periods. For example, Cassel et al. (2009) used a local empirically based lapse rate of -17.4 ‰/km (Ingraham and Taylor, 1991) for Cenozoic estimates of the paleoelevation of the northern Sierra Nevada, while, Hren et al. (2010), used the Rayleigh distillation model, where temperature and relative humidity for different paleo-climates were used as inputs to determine the paleo-lapse rates for Eocene paleo-elevation reconstructions in the northern Sierra Nevada. The best practices for paleoaltimetry remain uncertain, and the goal of this study is to better understand the limitations and opportunities provided by theoretical approaches based on Rayleigh distillation.

Both of these approaches rely on some combination of simple assumptions about atmospheric dynamics. Some common assumptions include: purely 2-D flow over topography (e.g. Poage and Chamberlain, 2001); air masses do not mix (e.g. Rowley, 2001); or that the isotopic lapse rate does not change significantly with changes in elevation or climate (e.g. Cassel et al., 2009). In a model of pure orographic precipitation, the incoming air is lifted, cooled, and the heavier isotopes are preferentially condensed and rained out along the windward path. Subsidence in the lee may then suppress further precipitation downstream. Atmosphere-mountain interactions are more complex than pure orographic precipitation, though. Pure orographic precipitation is rare, and few mountain ranges are dominated by simple upslope flow. More typically, precipitation is orographically enhanced within a larger scale weather system (e.g. Houze, 2012; Galewsky and Sobel, 2005). Changes in climate and atmospheric circulation can lead to a more complicated relationship between isotopic composition of precipitation and elevation (e.g. Molnar, 2010; Galewsky, 2008; Insel et al., 2012; Wheeler et al., 2016). It should be noted that paleoaltimetry studies recognize the limitations of both the theoretical and empirical approaches to interpreting paleoelevations and have tried to incorporate more complex atmospheric dynamics into their interpretations (e.g. Mulch, 2016; Winnick et al., 2014; Rowley, 2007).

3.2.1. Atmospheric modeling for isotope-based paleoaltimetry constraints

Recently there has been a push to investigate the relationship between the isotopic composition of precipitation and elevation using numerical models. General Circulation Models (GCMs) of modern and paleo-climates and idealized models of atmospheric flow over simplified ridges have shed light on the controls of this relationship, and the implications that has for isotope-based paleoaltimetry estimates. Several studies using GCMs with varying degrees of isotope-enabled tracing or microphysics schemes have been used to interpret paleoaltimetry isotope records (e.g. Poulsen et al., 2007; Insel et al., 2012; Feng et al., 2016; Herold et al., 2014). Each of these studies used GCMs to address some aspect of the change in isotopic composition of precipitation due to changes in elevation, climate, or land surface vegetation. GCMs have coarse resolution, though, with generally 0.5° to 2° of horizontal resolution. Coarse horizontal resolution smooths topography and the local atmospheric effects may then be muted. For example, with a 1° x 1° grid spacing, the modern Sierra Nevada are less than one grid point across and 4 to 5 grid points in length. This smoothing strongly influences the simulated atmospheric circulation and any orographically enhanced precipitation in the region. In a comparison of horizontal model resolution for the western United States, at lower resolutions, the coastal mountains are not resolved (Wang et al., 2004). The lower resolution affects temperatures, especially at high elevation, and the difference in temperature at high altitude creates significant differences in the hydrologic cycle. Although isotopes are not included in the model in Wang et al. (2004), it is possible that the differences in the hydrologic cycle between the simulations with different resolutions could affect the $\delta D_{precipitation}$.

Idealized models of atmospheric flow seek to systematically control atmospheric conditions and topography to determine how changes in elevation and climate affect the isotopic composition of precipitation. Models with (e.g. Galewsky, 2009; Moore et al., 2016) and without (e.g. Galewsky, 2008; Wheeler et al., 2016) isotope microphysics have investigated this relationship and found that changes in ridge height and climate can affect the windward and leeward isotopic composition of precipitation. Specifically, these changes in ridge height and climate lead to changes in flow deflection around a ridge.

Atmospheric flow over topography can be understood in terms of the nondimensional flow parameter Nh/U, where N is the Brunt-Väisälä frequency (s^{-1}), h is the mountain height (m), and U is the horizontal wind speed (m/s) (e.g. Epifanio and Durran, 2001). Idealized models of atmospheric flow around topographic barriers suggest that when $Nh/U \ll 1$, flow tends to pass over the topographic barrier, but when $Nh/U \gg 1$, flow tends to be deflected around the topographic barrier (Galewsky, 2008). When $Nh/U \gg 1$ windward lapse rates diverge from 1-D Rayleigh distillation models (Galewsky, 2009) and may impact leeside isotope records as well (Lechler and Galewsky, 2013; Wheeler et al., 2016). These studies (Galewsky, 2008; Galewsky, 2009; Moore et al., 2016; Wheeler et al., 2016) used simulations of upslope flow and pure orographic precipitation, despite the limitations described above. In this study we use a more realistic, although still idealized, meteorological forcing to better understand the links between weather systems, topography, and the isotopic composition of precipitation, and to compare these results with those obtained from a simple Rayleigh distillation model, with the aim of improving our understanding of the best approaches for paleoaltimetry studies.

Using an isotope enabled Weather Research and Forecasting model (WRF), we build on previous studies of atmospheric flow around idealized ridges by simulating the isotopic composition of orographically enhanced precipitation with changing elevation in an idealized winter-time storm. Through a relatively high resolution, 3-D simulation of a winter-time storm system we test the response of $\delta D_{precipitation}$ to changes in elevation and compare those results to a 1-D Rayleigh distillation model. The input conditions for the Rayleigh distillation model are based on the same atmospheric thermal structure within the WRF simulations so that we can directly compare lapse rates from Rayleigh distillation to lapse rates generated during a simulated winter-time storm.

3.3. Methods

Using the Weather Research and Forecasting (WRF) model version 3.5.1 (Skamarock et al., 2008) we incorporate a simplified isotope microphysics scheme into the Kessler microphysics scheme (Kessler, 1969). For our simulations, we used the idealized baroclinic wave simulation, a winter-time storm system that is common in the mid-latitudes. The model simulates a 3-D baroclinic wave within a baroclinically unstable jet in the northern hemisphere.

Isotope microphysics are added into the model by incorporating a 'perfect precipitation' model into the Kessler microphysics scheme, after Galewsky (2009). Two tracers are added to the model, one that represents all of the water vapor in the system, initialized to be equal to the initial water vapor mixing ratio set for the baroclinic wave simulation. The second tracer represents the mixing ratio of the heavy isotopologue of water vapor and is initialized so that at the surface δD_{vapor} = -100 ‰ vSMOW and decreases linearly to -300 ‰ vSMOW at the model top based on observations (Galewsky et al., 2016 and references therein). Once a grid point reaches saturation, the excess water vapor is condensed and falls out as precipitation. Fractionation takes place upon condensation according to the temperature-dependent equilibrium factors (Majoube, 1971; Merlivat and Nief, 1967).

We use a 25 km horizontal grid spacing on a domain of 320 x 160 points, with 64 unevenly spaced vertical levels extending to 16 km. The model domain covers an area roughly as wide as the continental United States from 0° to 80° latitude. The east-west boundary conditions are periodic, where the output from the eastern boundary is the input for the western boundary. The idealized ridge sits in the center of the domain and is 250 km wide by 1000 km long. We run 8 simulations with a uniform ridge with a maximum elevation that ranges from 1 to 4.5 km by 500 m increments. Each simulation is run for a total of 360 hours, the first 186 hours are regarded as model spin-up and are not included in our analyses.

The idealized baroclinic wave simulation in WRF has been used in previous studies with various initial conditions, model domain sizes, etc. (e.g. Park et al., 2014; Kim et al., 2016; Blázquez et al., 2013; Jablonowski and Williamson, 2006). None of these studies include isotope microphysics into the model, which leaves us with no direct comparison to validate our results. We compare our results to another baroclinic wave model with a more sophisticated microphysics scheme instead. Dütsch et al. (2016) used the COSMOiso model to simulate an idealized baroclinic wave. COSMOiso includes the heavy isotopes, δD and $\delta^{18}O$, and fractionation takes place upon any phase transition. This differs from our model where fractionation only takes place upon condensation. While the isotope scheme in COSMOiso is more sophisticated, our results from a control simulation without any topography show a similar spatial distribution and magnitude of change in the isotopic composition of precipitation (see Chapter 6 Supplemental Materials). This leads us to believe that our model is capturing the first-order controls on the isotopic composition of the precipitation.

For each simulation we calculate the windward $\delta D_{precipitation}$ lapse rate ($\delta D_{WRF\text{-}LR}$) from 186 hours to 360 hours. We define the windward face as the western face of the ridge up to the ridge crest. $\delta D_{WRF\text{-}LR}$ is the linear regression of the average $\delta D_{precipitation}$ at each elevation along the windward face, for the entire length of the ridge. For each simulation we also calculate a lapse rate from a Rayleigh distillation curve ($\delta D_{RD\text{-}LR}$). The inputs for the Rayleigh distillation calculation come directly from the WRF model. We use the average incoming temperature conditions for the length of the ridge from 186 hours to 360 hours. $\delta D_{RD\text{-}LR}$ is calculated using a linear regression from the start of saturation (~500 m) to the maximum elevation of the ridge.

3.4. Results

As ridge height increases, $\delta D_{WRF\text{-}LR}$ and $\delta D_{RD\text{-}LR}$ both generally steepen, and $\delta D_{RD\text{-}LR}$ is almost always steeper than $\delta D_{WRF\text{-}LR}$ (Figure 3.1). The $\delta D_{WRF\text{-}LR}$ generally steepen with increasing elevation where for the 1 km ridge $\delta D_{WRF\text{-}LR}$ = -4.6 ‰/km and for the 4 km ridge $\delta D_{WRF\text{-}LR}$ = -9.5 ‰/km, an increase of almost 5 ‰/km. The trend of steepening lapse rate with increasing elevation does not continue for the simulation with the 4.5 km ridge, $\delta D_{WRF\text{-}LR}$ = -6.5 ‰/km shallowing by almost 3 ‰/km. As in the WRF simulations, the $\delta D_{RD\text{-}LR}$ steepen with increasing elevation, from -1.4 ‰/km for the 1 km ridge to -21.5 ‰/km for the 4.5 km ridge.

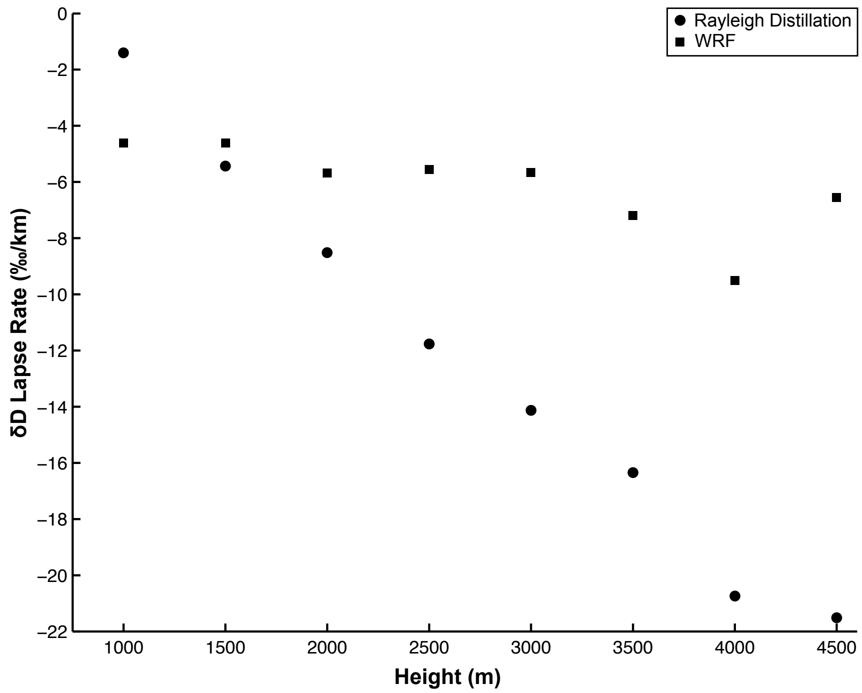

Figure 3.1. Comparison of lapse rates from the Rayleigh distillation model and WRF model. $\delta D_{WRF\text{-}LR}$ and $\delta D_{RD\text{-}LR}$ generally decrease while $\delta D_{RD\text{-}LR}$ is almost always lower than $\delta D_{WRF\text{-}LR}$. Circles – Rayleigh distillation. Squares – WRF.

The $\delta D_{RD\text{-}LR}$ is consistently lower than the $\delta D_{WRF\text{-}LR}$, with the exception of the 1 km ridge. In the 1 km ridge simulation there are several instances where the 6-hourly atmospheric conditions do not support condensation with the ascent of the air parcel for the altitudes of interest. This is not the case for any of the other simulations. The inclusion of these times in the average conditions for the Rayleigh distillation model shallows the $\delta D_{RD\text{-}LR}$ and explains the relationship between $\delta D_{WRF\text{-}LR}$ and $\delta D_{RD\text{-}LR}$ for the 1 km ridge simulation.

The input conditions for the Rayleigh distillation model come directly from the average conditions for each of the WRF simulations, yet, the $\delta D_{RD\text{-}LR}$ are generally steeper than the $\delta D_{WRF\text{-}LR}$. The lapse rates in both cases are determined by the temperature at condensation, the amount of condensation, and the δD_{vapor} structure. In order to determine what controls the difference in lapse rate between the Rayleigh distillation models and the WRF simulations, we compare the quantity of condensation and the δD_{vapor} structure between the two models.

For the Rayleigh distillation models we use the δD_{vapor} profile generated for the average incoming conditions for each simulation. For the WRF simulations, we select the δD_{vapor} at condensation along the windward side of the ridge from 6-hourly output between 186 hours to 360 hours and average the output for all times at each vertical level. To compare the quantity of condensation between the two models, we calculate the precipitation efficiency, the ratio of precipitation to the total water vapor for a vertical column multiplied by 100 (Market and Allen, 2003). For the Rayleigh distillation model we use the excess water vapor and total column water vapor generated from the average incoming conditions for each simulation. For the WRF simulations, we calculate the average precipitation efficiency along the entire windward face of the ridge from 186 hours to 360 hours. Any columns that do not generate precipitation are excluded from the average.

We find that the δD_{vapor} structure between the Rayleigh distillation models and the WRF simulations are similar at lower altitudes but begin to diverge from one another as the elevation of the ridge increases (not shown). While there are some differences in the δD_{vapor} structure between the Rayleigh distillation models and the WRF simulations, we do not believe that the difference in δD_{vapor} structure is what controls the difference in lapse rates. Our analysis of precipitation efficiency on the other hand finds that there are significant differences between the WRF simulations and the Rayleigh distillation models. The Rayleigh distillation models are significantly more efficient than the WRF simulations (Table 1). This is consistent with other studies that compare precipitation efficiency of Rayleigh distillation to other processes (e.g. Bony et al., 2008).

Ridge height (m)	WRF (%)	Rayleigh Distillation (%)
1000	0.038	3.41
1500	0.062	3.59
2000	0.085	3.83
2500	0.120	4.08
3000	0.167	4.44
3500	0.186	4.81
4000	0.254	5.11
4500	0.266	4.85

Table 3.1. Precipitation efficiency for the WRF simulations and the Rayleigh distillation model. Precipitation efficiency in the Rayleigh distillation model is significantly greater than in the WRF simulations.

Our results suggest that the difference in the lapse rates between the WRF simulation and Rayleigh distillation is most likely due to the difference in precipitation efficiency between the two models. The precipitation efficiency is high in the Rayleigh distillation models because there is more excess water vapor and total water vapor in the column. In Rayleigh distillation models the relative humidity is 100% throughout the column. As the air parcel ascends to cooler temperatures the relative humidity exceeds 100% and condenses out the excess water vapor. Condensing out the excess water vapor returns the relative humidity back to 100% before ascending to the next level and repeating the process.

In the WRF simulations the relative humidity throughout a column can vary and will not always exceed 100% or generate condensation (Figure 3.2). The representative columns i-iv in Figure 3.2A demonstrate the difference in relative humidity and condensation within the WRF model along the windward side. The altitude of condensation can vary and does not take place throughout the entire column as it does in Rayleigh distillation models. In Figure 3.2A for column i, there is no condensation throughout the column, as the relative humidity does not exceed 100%. In Figure 3.2A for column ii, some condensation is forming at low altitudes within the column but above 2 km the relative humidity does not exceed 100%. In Figure 3.2A for column iii, condensation is forming below and above the maximum elevation of the ridge crest but above 4.5 km, and for a small region around 3.5 km, the relative humidity does not exceed 100%. In Figure 3.2A for column iv, the relative humidity is high and condensation is forming throughout the column up to 6 km.

Figure 3.2 also illustrates two scenarios, one where we would expect steeper lapse rates (Figure 3.2A) and another where we would expect shallower lapse rates (Figure 3.2B). In Figure 3.2A there is little or no condensation forming at lower elevations and more condensation forming at higher elevations along the ridge. This would suggest that with increasing elevation on the windward side of the ridge the lapse rate should be relatively steep. In Figure 3.2B, condensation is forming at roughly the same altitude across the entire windward side of the ridge. This would suggest that for each location the $\delta D_{precipitation}$ does no change significantly with altitude and the lapse rate should be shallower in comparison to Figure 3.2A.

While the WRF simulations undergo both of the scenarios illustrated in Figure 3.2, the Rayleigh distillation models do not. It is the high precipitation efficiency within a closed system for the Rayleigh distillation models, and the fact that condensation forms at varying altitudes within the WRF simulations, an open system, that accounts for the difference in lapse rates between the WRF simulations and Rayleigh distillation models. Consider two air masses with the same δD_{vapor}. The air mass that condenses out more water vapor has a greater change from δD_{vapor} to $\delta D_{precipitation}$. If this continues, where one of the air masses is progressively raining out more than the other, the overall change in $\delta D_{precipitation}$ will be greater. We suggest that due to the high precipitation efficiency that Rayleigh distillation should always produce the steepest lapse rates.

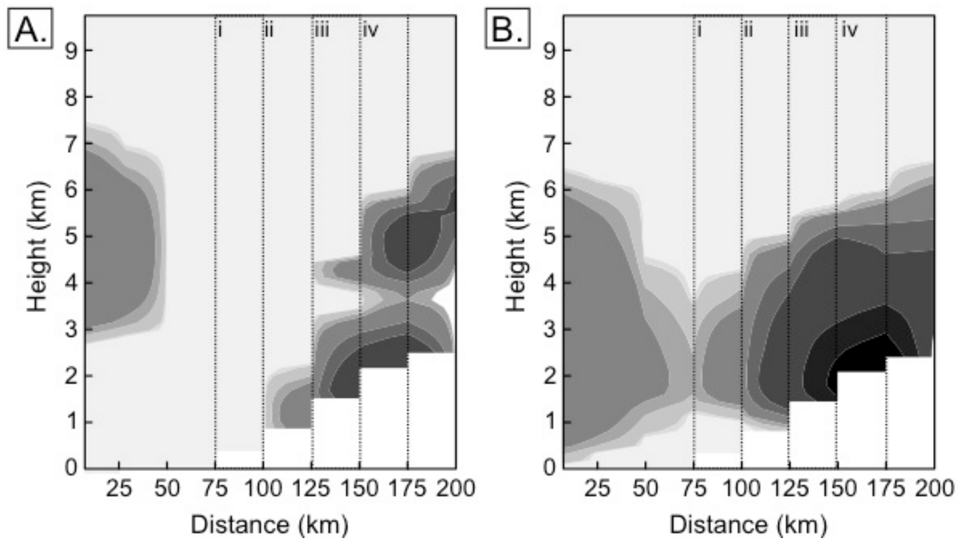

Figure 3.2. Illustrative cross section of windward condensation for a 2.5 km ridge. Dark colors represent high condensation and light colors represent low condensation. Figure 2A represents a scenario in which we would expect steep lapse rates, where there is little or no condensation forming at lower elevations and more condensation forming at higher elevations along the ridge. A.i.) There is no condensation throughout the column as the relative humidity does not exceed 100%. A.ii.) Some condensation is forming at low altitudes within the column but above 2 km the relative humidity in this column does not exceed 100% and therefore no precipitation is generated above 2 km. A.iii.) Condensation is forming below and above the maximum elevation of the ridge crest but above 4.5 km and for a small region around 3.5 km the relative humidity does not exceed 100% and therefore is no condensation in these regions. A.iv.) The relative humidity is high and condensation is forming throughout the column up to 6 km. Figure 2B represents a scenario in which we would expect shallower lapse rates. B.i-iv.) Condensation is forming at roughly the same altitudes across the entire windward side of the ridge.

3.5. Discussion

From our simulations of a winter-time storm system around an idealized ridge we find that lapse rates for both the WRF simulations and Rayleigh distillation models generally steepen with increasing elevation. Lapse rates from the Rayleigh distillation model are almost always steeper than the lapse rates from the WRF simulations and as the elevation of the ridge increases, the difference between the δD_{WRF-LR} and δD_{RD-LR} increases. We suggest that the difference between the δD_{WRF-LR} and δD_{RD-LR} is most likely the result of increased precipitation efficiency in Rayleigh distillation models relative to the WRF simulations. While the $\delta D_{precipitation}$ is controlled by the same factors for both the Rayleigh distillation model and the WRF simulations, the lapse rates are very different. This is due to the fact that in the WRF simulations when precipitation is generated the excess water vapor does not come from the entire column of air directly above that point. Instead only some of the column exceeds a relative humidity of 100% and generates precipitation. In Rayleigh distillation models, the entire column exceeds a relative humidity of 100% and generates precipitation.

Previous studies have focused on the changes in elevation and climate for models of pure upslope flow and found that with increasing elevation lapse rates diverge from Rayleigh distillation models (Galewsky 2009). Our results support these findings and continue to demonstrate that in 3-D models of orographically enhanced precipitation with increasing elevation, simulated lapse rates diverge from Rayleigh distillation models even when controlling for the atmospheric conditions.

3.5.1. Implications for isotope-based paleoaltimetry

A difference in the isotope lapse rate has the potential to significantly alter paleoaltimetry interpretations. If we use the WRF simulations and the Rayleigh distillation models in this study as an example, Rayleigh distillation would significantly under-estimate the topography for all of the WRF simulations with the exception of the 1 km ridge. For the 2.5 km ridge the Rayleigh distillation model would under-estimate the elevation in the WRF simulation by 2 km. For every ridge with an elevation of 1.5 km or greater, the Rayleigh distillation approach would suggest that the ridge height in the WRF simulation does not exceed 1 km. This difference in estimated height becomes an issue above 1.5 km as the difference in the ridge height in the WRF simulations and the difference in the estimated ridge height from Rayleigh distillation models exceeds 1 km. If we were applying this to interpretations of the paleo-elevation of a mountain range we would under-estimate the elevation of the topography, which would potentially lead to over-estimating the amount of surface uplift over the period of interest.

While the isotopic composition of precipitation within a mountain range is generated by more complex atmospheric dynamics, since Rayleigh distillation models should produce the steepest lapse rates, they may be useful in determining the minimum elevation bounds and maximum uplift bounds for a time of interest. If the temperature conditions can be constrained using techniques such as clumped oxygen isotopes (Eiler, 2011), and in conditions where flow deflection is relatively low, the Rayleigh distillation model should yield the steepest possible lapse rate for those conditions providing a minimum elevation bound and maximum uplift bound.

Empirical and theoretical studies are based on longer-term averages, but do not always have controls on how increasing height or changes in climate impacts the $\delta D_{precipitation}$ and the resulting lapse rate. While we recognize that we may not be representing all the complexity of the isotopic system in our model since we are only looking at winter-time precipitation over a relatively short time period and are using a simplified isotope microphysics scheme, this is a first step to comparing lapse rates from Rayleigh distillation to orographically enhanced flow and determining the controls on windward isotopic lapse rates and our results suggest that Rayleigh distillation may be better used as a minimum boundary of elevation and a maximum boundary of uplift.

3.6. Conclusions

The goal of this paper was to establish a relationship between elevation and the $\delta D_{precipitation}$ for orographically enhanced precipitation in an idealized winter-time storm and compare the results with Rayleigh distillation models for the same atmospheric conditions. We find that lapse rates for both the WRF simulations and Rayleigh distillation models generally decrease with increasing elevation but that the lapse rates from the Rayleigh distillation model are almost always steeper than the lapse rates from the WRF simulations due to the high precipitation efficiency in Rayleigh distillation models. We suggest that Rayleigh distillation models may produce the steepest possible lapse rates for a given thermal structure and may be a useful technique for determining the minimum elevation of a mountain range and the maximum amount of uplift, provided that paleo-climate conditions can be accurately constrained.

3.7. References in Chapter 3

Blázquez, J., Pessacg, N.L., and Gonzalez, P.L.M., 2013, Simulation of a baroclinic wave with the WRF regional model: sensitivity to the initial conditions in an ideal and a real experiment: Meteorological Applications, v. 20, p. 447–456, doi: 10.1002/met.1307.

Bony, S., Risi, C., and Vimeux, F., 2008, Influence of convective processes on the isotopic composition ($\delta^{18}O$ and δD) of precipitation and water vapor in the tropics: 1. Radiative-convective equilibrium and Tropical Ocean – Global Atmosphere – Coupled Ocean-Atmosphere Response Experiment (TOGA-C: Journal of Geophysical Research, v. 113, doi: 10.1029/2008JD009942.

Cassel, E.J., Graham, S. a., and Chamberlain, C.P., 2009, Cenozoic tectonic and topographic evolution of the northern Sierra Nevada, California, through stable isotope paleoaltimetry in volcanic glass: Geology, v. 37, p. 547–550, doi: 10.1130/G25572A.1.

Dansgaard, W. (1964), Stable isotopes in precipitation, Tellus, 16, 436– 468.

Dütsch, M., Pfahl, S., and Wernli, H., 2016, Drivers of δ^2H variations in an idealized extratropical cyclone: Geophysical Research Letters, v. 43, p. 5401–5408, doi: 10.1002/2016GL068600.1.

Eiler, J.M., 2011, Paleoclimate reconstruction using carbonate clumped isotope thermometry: Quaternary Science Reviews, v. 30, p. 3575–3588, doi: 10.1016/j.quascirev.2011.09.001.

Epifanio, C.C., and Durran, D.R., 2001, Three-Dimensional Effects in High-Drag-State Flows over Long Ridges: Journal of the Atmospheric Sciences, v. 58, p. 1051–1065, doi: 10.1175/1520-0469(2001)058<1051:TDEIHD>2.0.CO;2.

Feng, R., Poulsen, C.J., and Werner, M., 2016, Tropical circulation intensification and tectonic extension recorded by Neogene terrestrial $\delta^{18}O$ records of the western United States: Geology, v. 44, p. 971–974, doi: 10.1130/G38212.1.

Galewsky, J., 2008, Orographic Clouds in Terrain-Blocked Flows: An Idealized Modeling Study: Journal of the Atmospheric Sciences, v. 65, p. 3460–3478, doi: 10.1175/2008JAS2435.1.

Galewsky, J., 2009, Orographic precipitation isotopic ratios in stratified atmospheric flows: Implications for paleoelevation studies: Geology, v. 37, p. 791–794, doi: 10.1130/G30008A.1.

Galewsky, J., and Sobel, A., 2005, Moist Dynamics and Orographic Precipitation in Northern and Central California during the New Year's Flood of 1997: Monthly

Weather Review, v. 133, p. 1594–1612, doi: 10.1175/MWR2943.1.

Galewsky, J., Steen-Larsen, H.C., Field, R.D., Worden, J., Risi, C., and Schneider, M., 2016, Stable isotopes in atmospheric water vapor and applications to the hydrologic cycle: Reviews of Geophysics, v. 54, doi: 10.1002/2015RG000512.Received.

Herold, N., Buzan, J., Seton, M., Goldner, A., Green, J.A.M., Müller, R.D., Markwick, P., and Huber, M., 2014, A suite of early Eocene (~ 55 Ma) climate model boundary conditions: Geoscientific Model Development, v. 7, p. 2077–2090, doi: 10.5194/gmd-7-2077-2014.

Houze, R.A., 2012, Orographic Effects on Precipitating Clouds: , p. 1–47, doi: 10.1029/2011RG000365.1.INTRODUCTION.

Hren, M.T., Pagani, M., Erwin, D.M., and Brandon, M., 2010, Biomarker reconstruction of the early Eocene paleotopography and paleoclimate of the northern Sierra Nevada: Geology, v. 38, p. 7–10, doi: 10.1130/G30215.1.

Ingraham, N.L., and Taylor, B.E., 1991, Light Stable Isotope Systematics of Large-Scale Hydrologic Regimes in California and Nevada: Water Resources Research, v. 27, p. 77–90.

Insel, N., Poulsen, C.J., Ehlers, T.A., and Sturm, C., 2012, Response of meteoric $\delta^{18}O$ to surface uplift: Implications for Cenozoic Andean Plateau growth: Earth and Planetary Science Letters, v. 317–318, p. 262–272, doi: 10.1016/j.epsl.2011.11.039.

Jablonowski, C., and Williamson, D.L., 2006, A baroclinic instability test case for atmospheric model dynamical cores: Quarterly Journal of the Royal Meteorological Society, v. 132, p. 2943–2975, doi: 10.1256/qj.06.12.

Kessler, E., 1969. On the Distribution and Continuity of Water Substance in Atmospheric Circulations. Meteorol. Monogr., 10(32), 88 pp.

Kim, Y.-H., Chun, H.-Y., Park, S.-H., Song, I.-S., and Choi, H.-J., 2016, Characteristics of gravity waves generated in the jet-front system in a baroclinic instability simulation: Atmospheric Chemistry and Physics, v. 16, p. 4799–4815, doi: 10.5194/acp-16-4799-2016.

Lechler, A.R., and Galewsky, J., 2013, Refining paleoaltimetry reconstructions of the Sierra Nevada: California, using air parcel trajectories: Geology, v. 41, p. 259–262, doi: 10.1130/G33553.1.

Majoube, M., 1971: Fractionation of oxygen 18 and of deuterium between water and its vapor. Journal of Chemical Physics, v. 68, p.1423–1436.

Market, P., and Allen, S., 2003, Precipitation Efficiency of Warm-Season Midwestern

Mesoscale Convective Systems: Weather and Forecasting, v. 18, p. 1273–1285.

Merlivat, L. and G. Nief, 1967: Isotopic fractionation of the solid-vapor and liquid-vapor changes of state of water at temperatures below 0°C. Tellus, v. 19, p.122–127.

Molnar, P., 2010, Deuterium and oxygen isotopes, paleoelevations of the Sierra Nevada, and Cenozoic climate: Bulletin of the Geological Society of America, v. 122, p. 1106–1115, doi: 10.1130/B30001.1.

Moore, M., Blossey, P.N., Muhlbauer, A., and Kuang, Z., 2016, Microphysical controls on the isotopic composition of winter-time orographic precipitation: Journal of Geophysical Research: Atmospheres, v. 121, p. 7235–7253, doi: 10.1002/2015JD023763.The.

Mulch, A., 2016, Stable isotope paleoaltimetry and the evolution of landscapes and life: Earth and Planetary Science Letters, v. 433, p. 180–191, doi: 10.1016/j.epsl.2015.10.034.

Park, S.-H., Klemp, J.B., and Skamarock, W.C., 2014, A Comparison of Mesh Refinement in the Global MPAS-A and WRF Models Using an Idealized Normal-Mode Baroclinic Wave Simulation: Monthly Weather Review, v. 142, p. 3614–3634, doi: 10.1175/MWR-D-14-00004.1.

Poage, M.A., and Chamberlain, C.P., 2001, Empirical relationships between elevation and the stable isotope composition of precipitation and surface waters: Considerations for studies of paleoelevation change: American Journal of Science, v. 301, doi: 10.2475/ajs.301.1.1.

Poulsen, C.J., Sciences, G., Arbor, A., and Pollard, D., 2007, General circulation model simulation of the $\delta^{18}O$ content of continental precipitation in the middle Cretaceous: A model-proxy comparison: , p. 199–202, doi: 10.1130/G23343A.1.

Rowley, D.B., 2007, Stable Isotope-Based Paleoaltimetry: Theory and Validation: Reviews in Mineralogy and Geochemistry, v. 66, p. 23–52, doi: 10.2138/rmg.2007.66.2.

Skamarock, W.C., Klemp, J.B., Dudhi, J., Gill, D.O., Barker, D.M., Duda, M.G., Huang, X.-Y., Wang, W., and Powers, J.G., 2008, A Description of the Advanced Research WRF Version 3: NCAR Technical Note, v. Tech. Note, p. 113, doi: 10.5065/D6DZ069T.

Wang, Y., Leung, L.R., Lee, D.-K., Wang, W.-C., and Ding, Y., 2004, Regional Climate Modeling: Progress, Challenges, and Prospects: Journal of the Meteorological Society of Japan, v. 82, p. 1599–1628.

Wheeler, L.B., Galewsky, J., Herold, N., and Huber, M., 2016, Late Cenozoic surface uplift of the southern Sierra Nevada (California, USA): A paleoclimate perspective on lee-side stable isotope paleoaltimetry: Geology, p. 451–454, doi: 10.1130/G37718.1.

Winnick, M.J., Chamberlain, C.P., Caves, J.K., and Welker, J.M., 2014, Quantifying the Isotopic “Continental Effect”: Earth and Planetary Science Letters, v. 406, p. 123–133, doi: 10.1016/j.epsl.2014.09.005.

4. LEESDIE ISOTOPE-BASED PALEOALTIMETRY IN THE NEW ZEALAND SOUTHERN ALPS: THE ROLE OF ATMOSPHERIC FLOW DEFLECTION

4.1. Abstract

The development of relief may generate leeside rain shadows where $\delta^{18}O$ values are lower due to rainout on the windward side. The magnitude of lowering in paleo-$\delta^{18}O$ sampled from the leeside of a mountain range should, at least in principle, be related to the elevation of the mountain range. In order for leeside proxies to record the highest elevations, atmospheric flow deflection around the mountain range needs to be minimal. Using the Weather Research and Forecasting model and Hybrid Single-Particle Lagrangian Integrated Trajectory (HYSPLIT) model, we demonstrate that modern atmospheric flow patterns in the Southern Alps of New Zealand are not dominated by flow deflection. The lack of flow deflection around the Southern Alps and the relatively simple uplift history supports the use of leeside isotope records to constrain the timing of uplift, and that uplift likely occurred ~5 Ma based on leeside isotope records. Orogens like the Sierra Nevada, that are characterized by high elevations and strong flow deflection, may not be good candidates for leeside isotope-based paleoaltimetry studies. Ideal candidates for leeside isotope-based paleoaltimetry studies should be characterized by relatively low elevations, low atmospheric flow deflection, and a simple uplift history.

4.2. Introduction

Topography develops as a result of the interaction between tectonics, surface processes, and climate, and can yield insight into the geodynamic evolution of a mountain range. Global $\delta^{18}O$ data from meteoric water show a linear relationship between net elevation and $\Delta\delta^{18}O$ on the windward side of a mountain range, where $\delta^{18}O$ values decrease as net elevation increases (Poage and Chamberlain, 2001). Leeside isotope-based paleoaltimetry was first proposed by Chamberlain et al. (1999) as means to constrain the timing of uplift for the Southern Alps of New Zealand. The development of relief may generate leeside rain shadows, where $\delta^{18}O$ values are lower due to rainout on the windward side. The magnitude of lowering in isotopic values in paleo-$\delta^{18}O$ sampled from the leeside of a mountain range should, at least in principle, be related to the elevation of the mountain range.

The Southern Alps are located along the Australian-Pacific plate boundary where most of the deformation of the collision of the Pacific and Australian plates is taken up along the Alpine fault (Norris and Cooper, 2001). Deformation along the Alpine fault is primarily dominated by oblique-slip and the Southern Alps are characterized by high erosion rates (up to 9 mm/yr) (Clarke and Burbank, 2010; Hovius et al., 1997; Griffiths, 1981; Hicks et al., 1996) and high uplift rates (6-8 mm/yr) (Tippett and Kamp, 1993; Batt et al., 2000; Herman et al., 2010). Several lines of geologic evidence suggest that the modern tectonic regime of oblique-slip and uplift in the Southern Alps evolved over the last ~5 Ma (Sutherland, 1995; Walcott, 1998; Batt et al., 2000). Leeside isotope-based paleoaltimetry records from the Southern Alps support the timing of uplift in these studies (Chamberlain et al., 1999). Within authigenic kaolinites collected on the leeside of the Southern Alps, there is a 5-6‰ decrease in $\delta^{18}O$ around 5 Ma. This suggests that a rain shadow developed ~5 Ma and prior to ~5 Ma, the Southern Alps were a relatively low topographic feature (Chamberlain et al., 1999).

One of the major, if implicit, assumptions in leeside isotope-based paleoaltimetry models is that atmospheric flow around and a mountain range is 2-D, implying that leeside isotope records come from air masses that have traveled W-E and surmounted the range crest. Atmospheric flow over topography can be understood, to first order, in terms of the nondimensional flow parameter *Nh/U*; where *N* is the Brunt-Väisälä frequency (s^{-1}), *h* is the mountain height (m), and *U* is the horizontal wind speed (m/s) (e.g., Epifanio and Durran, 2001). Idealized models of atmospheric flow around topographic barriers suggest that when $Nh/U \ll 1$, flow tends to pass over the topographic barrier, but when $Nh/U \gg 1$, flow tends to be deflected around the topographic barrier (Galewsky, 2009). In order for leeside proxies to record the highest elevations, *Nh/U* needs to be relatively low.

Interpretations of leeside isotope-based paleoaltimetry records for the California Sierra Nevada (Poage and Chamberlain, 2000) do not agree with other lines of geologic evidence for the timing of uplift of the Sierra Nevada (Wakabayashi, 2013 and references therein) as they do for the Southern Alps. This is due to the fact that the modern atmospheric conditions in the Sierra Nevada are dominated by flow deflection (Lechler and Galewsky, 2013) and the atmospheric flow patterns during the Miocene were likely dominated by flow deflecion as well (Mulch, 2016; Wheeler et al., 2016). While flow deflection may have dominated Miocene flow patters for the southern Sierra Nevada, leeside isotope-based paleoaltimetry would not be able to distinguish whether or not the establishment of flow deflection was due to the elevation or climate during this time (Wheeler et al., 2016). This may account for the difference in interpretation between the leeside isotope records and other lines of geologic evidence.

Chamberlain et al. (1999) suggests that flow in the Southern Alps is dominated predominantly by westerly winds and that these flow patterns have persisted through time, making the region a good candidate for leeside isotope-based paleoaltimetry. Using the Weather Research and Forecasting model (WRF) model and the Hybrid Single-Particle Lagrangian Integrated Trajectory (HYSPLIT) model we investigate the extent to which atmospheric flow patterns in the Southern Alps may be dominated by flow deflection and try to establish what makes a mountain range a good candidate for leeside isotope-based paleoaltimetry.

4.3. Methods

Using the WRF model v3.5.1 (Skamarock et al., 2008), we downscale the 1° x 1° horizontal resolution National Centers for Environmental Protection FNL (Final) Operational Global Analysis (NCEP FNL) to a 12 km grid for a five year period from 2009 to 2013. We use the downscaled, higher-resolution WRF output as input to the HYSPLIT (Stein et al., 2015) trajectory model, and run both forward and back-trajectories for the Southern Alps. We run a nested simulation, where a larger, parent domain encompasses a smaller nested domain. The model domain is centered on -40° S and 173° W. The parent domain is 149 grid points in both the W-E and N-S directions with 36 km grid spacing and 29 vertical levels extending to 50 hPa. The nested domain is 120 grid points in both the W-E and N-S directions with 12 km grid spacing and 29 vertical levels extending to 50 hPa. We use the WRF single moment 6-phase (WSM6) microphysics scheme for our simulation (Hong et al., 2004).

We run forward trajectories for 6 locations immediately offshore along the west coast of the South Island along the Southern Alps and back-trajectories for two locations on the leeside of the Southern Alps (Figure 4.1). Based on the sampling locations in Chamberlain et al. (1999), we select Chatto Creek and Glentanner as our back-trajectory starting points. For both the forward and back-trajectories, we calculate 12-hour trajectories at 6-hour intervals between 2009 and 2013. At each location a trajectory is initiated at 500, 1000, and 1500 m above sea level.

After Hughes et al. (2008) we calculate the average offshore incoming Nh/U from 2009 to 2013. We define the incoming offshore region as the area between the coast and 60 km to the west between -42° S and -45.7° S. We use the average N_m and incoming wind speeds, from the model surface to 400 hPa, and the average height of the Southern Alps at 12 km resolution for h. We exclude any winds where both U and V are negative from the average. For the back-trajectories we calculate Nh/U just before the trajectory makes landfall. If a back-trajectory does not reach the ocean we calculate Nh/U for the end point of the trajectory. N_m and the wind speeds are averaged from the model surface to 400 hPa. For h we use the maximum terrain height that the trajectory passes over along its path to the leeside location.

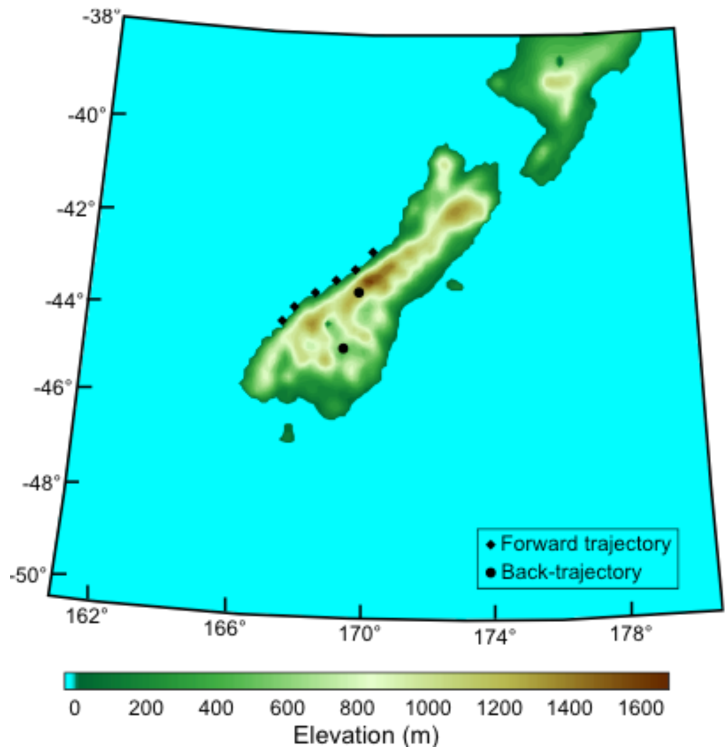

Figure 4.1. 12 km resolution model domain and trajectory locations. Contour fill values define the elevation (m) of the model terrain. The initial forward and back-trajectory locations are indicated with diamonds and circles, respectively.

4.4. Trajectory and *Nh/U* Results

From our forward trajectory analysis, 75% of the trajectories cross the Southern Alps into the leeside during the five year period from 2009 to 2013. The average maximum elevation that a forward trajectory surmounts on its path to the leeside is 1,026 m, and 48% of the trajectories surmount elevations ≥ 1,098 m, the average elevation of the Southern Alps. For the year 2013, we ran the simulation with two nested domains, where within the 12 km nested domain there was a 4 km nested domain within it. For the higher resolution domain, only forward trajectories were run. We find that 67% of the forward trajectories cross the Southern Alps and surmount an average maximum elevation of 1,140 m along the path to the leeside. While this is lower than the average for the 12 km resolution domain from 2009-2013, it still suggests that the majority of air masses are crossing over the Southern Alps along their path to the leeside.

The average incoming *Nh/U* from 2009-2013 is 1.32, where $N_m = 0.0080\ s^{-1}$, $U = 6.7$ m/s, and $h = 1{,}098$ m. While this is not significantly greater than 1, *Nh/U* is still relatively high and might initially suggest that flow deflection dominates atmospheric flow patterns in the Southern Alps, the results of our back-trajectory analysis suggests otherwise.

Air parcel trajectory pathways for the leeside locations are presented in the form of trajectory contour plots (Figure 4.2). 79% of precipitating trajectories (n = 3227) cross the Southern Alps along their path to Glentanner. Those that reach Glentanner and surmount the Southern Alps, cross over an average terrain height of 1,292 m with an average *Nh/U* of 0.94. 81% of precipitating trajectories (n = 1125) cross the Southern Alps along their path to Chatto Creek. Those that reach Chatto Creek and surmount the Southern Alps, cross over an average terrain height of 943 m with an average *Nh/U* of 0.81.

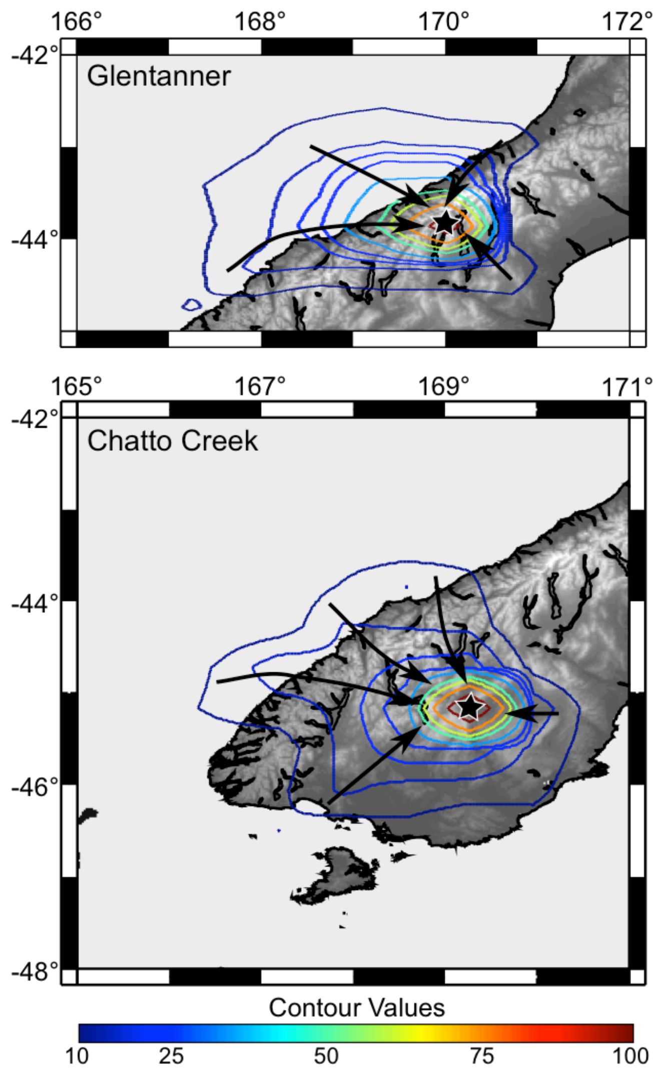

Figure 4.2. Back-trajectory contour plots for Glentanner and Chatto Creek. Contour values quantify how frequently an air parcel travels above a point on Earth's surface, stars mark the location of the back-trajectory point, and black arrows illustrate dominant air parcel transport pathways.

4.5. Discussion

From our trajectory analyses we find that there is relatively little flow deflection in the Southern Alps in the modern climate. The results of our back-trajectory analysis suggest that about 80% of precipitating air masses that reach the leeside locations originate from the west and cross the Southern Alps. Our forward trajectory analysis provides additional evidence that air masses are crossing over the Southern Alps on their path to the leeside. Our calculations of *Nh/U* are also consistent with the lack of flow deflection in the Southern Alps, where for precipitating back-trajectories for two locations on the leeside, *Nh/U* < 1. Our results are supported by previous studies of stable water isotopologues in the Southern Alps, which found that in the central-northern Southern Alps, when there is precipitation at Hokitika, wind directions were predominantly northwesterly (Kerr et al., 2015).

One question that still remains is whether or not flow deflection could have dominated atmospheric flow patterns during the Miocene. For warmer and wetter Miocene atmospheric conditions, we would expect for N_m to increase relative to modern values as it does in the Sierra Nevada (e.g. Wheeler et al., 2016). Assuming that the incoming offshore winds did not change significantly during the Miocene and elevation remained the same, *Nh/U* would be slightly increased relative to modern values. If we assume that the average elevation of the Southern Alps was lower during the Miocene, *Nh/U* would likely be lower than modern values. Both the modern and Miocene *Nh/U* for the Southern Alps are likely low making it more likely that air masses would flow over the terrain and that leeside precipitation would contain a record of elevation over this time.

Leeside isotope-based paleoaltimetry has been used in other mountain ranges, such as the Sierra Nevada (Chamberlain and Poage, 2000; Mulch, 2016; Chamberlain et al., 2012) where the timing of 1-2 km of uplift in the southern Sierra Nevada has been debated based on different lines of geologic evidence. While the leeside isotope record in the Southern Alps agrees well with other lines of geologic evidence for the timing of uplift (Batt, 2001 and references therein), the leeside isotope record over the last 18 Ma in the southern Sierra Nevada do not (Wakabayashi, 2013 and references therein). Early interpretations of leeside isotope records in the southern Sierra Nevada suggest that the lack of change of precipitation δ-values over time indicated that there may have been relatively little surface uplift since 18 Ma (Poage and Chamberlain, 2002; Crowley et al., 2008). More recent interpretations (e.g. Mulch, 2016; Chamberlain et al., 2012) suggest that the southern Sierra Nevada may have been sufficiently high to induce similar-to-modern flow patterns since 12.1 Ma (Mulch, 2016). In some cases this interpretation contradicts other lines of geologic evidence that argue for a low Miocene southern Sierra Nevada (e.g. Wakabayashi, 2013).

Modern trajectory analyses for locations on the leeside of the Sierra Nevada find that flow is diverted around, rather than over, the highest topography (Lechler and Galewsky, 2013). This is especially true in the southern Sierra Nevada, where deflection dominates the flow path for areas above 2.5 km. Whether or not flow deflection persisted in the southern Sierra Nevada during the Miocene is crucial to interpreting leeside isotope-based paleoaltimetry records. Models of atmospheric flow for idealized configurations of the Sierra Nevada suggest that similar-to-modern atmospheric flow patterns could have been established in the southern Sierra Nevada for lower elevations in a Miocene climate (Wheeler et al., 2016). While leeside records may show an establishment of flow deflection around the southern Sierra Nevada (Mulch, 2016), it can not be determined whether or not those flow patterns were developed due to changes in climate or elevation. As a result, leeside isotope records may not be able to constrain the magnitude or timing of uplift of the southern Sierra Nevada over the last 18 Ma (Wheeler et al., 2016).

Based on our comparison of leeside isotope-based paleoaltimetry in the Southern Alps and the southern Sierra Nevada, we suggest that interpretations of the uplift history of a mountain range based on leeside records should consider atmospheric flow patterns and the complexity of the uplift history before attempting to interpret changes in δ-values as changes in elevation. The lack of modern, and likely Miocene, flow deflection in the Southern Alps supports the work of Chamberlain et al. (1999) and suggests that leeside proxies of meteoric waters should record the development of a rain shadow with the uplift of the Southern Alps. This is not the case for all leeside isotope-based paleoaltimetry studies though. Mountain ranges with much higher average elevations, greater than 2-2.5 km, may experience more flow deflection in a modern climate and may not be good candidates for leeside isotope-based paleoaltimetry studies if flow deflection dominated flow patterns in the past (Galewsky and Lechler, 2013; Wheeler et al., 2016).

Due to the relatively high elevation of the southern Sierra Nevada and the complex uplift history, isotope-based paleoaltimetry may not be able to differentiate between the two proposed models of uplift. Where the first model proposes two pulses of 1 km of surface uplift over 20 Ma versus the second model, which proposes an already high mountain range with only 1 km of surface uplift over 20 Ma. In contrast, regions like the Southern Alps may be ideal candidates for leeside isotope-based paleoaltimetry studies because the following characteristics are met: (1) relatively low elevations and commensurately low values of Nh/U; and (2) relatively simple uplift histories consisting of essentially a single period of surface uplift from an initially low-relief surface.

4.6. Conclusions

In the Southern Alps, simulations of modern atmospheric flow between 2009 and 2013 were associated with little flow deflection, and most air parcels reached the leeside by traversing over the Southern Alps rather than being deflected around. The lack of atmospheric flow deflection in both the modern and Miocene climate suggests that leeside isotope-based paleoaltimetry records should record the timing of uplift of the Southern Alps. This study supports the work in Chamberlain et al. (1999) and suggests that leeside isotope records should record the aridification associated with the increase in surface uplift of the Southern Alps and suggests that the Southern Alps were a topographic feature ~5 Ma. Based on the results presented here and those of Wheeler et al. (2016), we suggest that leeside isotope-based paleoaltimetry is best applied in relatively low-lying mountain ranges with relatively simple uplift histories, and where atmospheric flow patterns are not dominated by flow deflection.

4.7. References in Chapter 4

Batt, G.E., 2001, The approach to steady-state thermochronological distribution following orogenic development in the Southern Alps of New Zealand: American Journal of Science, v. 301, p. 374–384.

Batt, G.E., Braun, J., Kohn, B.P., and McDougall, I., 2000, Thermochronological analysis of the dynamics of the Southern Alps, New Zealand: GSA Bulletin, v. 112, p. 250–266.

Chamberlain, C.P., Mix, H.T., Mulch, A., Hren, M.T., Kent-corson, M.L., Davis, S.J., Horton, T.W., and Graham, S.A., 2012, The Cenozoic Climate and Topographic Evolution of the Western North American Cordillera: v. 312, p. 213–262, doi: 10.2475/02.2012.05.

Chamberlain, C.P., and Poage, M.A., 2000, Reconstructing the paleotopography of mountain belts from the isotopic composition of authigenic minerals: Geology, v. 28, p. 115–118, doi: 10.1130/0091-7613(2000)28<115:RTPOMB>2.0.CO.

Chamberlain, C.P., Poage, M.A., Craw, D., and Reynolds, R.C., 1999, Topographic development of the Southern Alps recorded by the isotopic composition of authigenic clay minerals, South Island, New Zealand: Chemical Geology, v. 155, p. 279–294, doi: 10.1016/S0009-2541(98)00165-X.

Clarke, B.A., and Burbank, D.W., 2010, Bedrock fracturing, threshold hillslopes, and limits to the magnitude of bedrock landslides: Earth and Planetary Science Letters, v. 297, p. 577–586, doi: 10.1016/j.epsl.2010.07.011.

Crowley, B.E., Koch, P.L., and Davis, E.B., 2008, Stable isotope constraints on the elevation history of the Sierra Nevada Mountains, California: GSA Bulletin, v. 120, p. 588–598, doi: 10.1130/B26254.1.

Epifanio, C.C., and Durran, D.R., 2001, Three-Dimensional Effects in High-Drag-State Flows over Long Ridges: Journal of the Atmospheric Sciences, v. 58, p. 1051–1065, doi: 10.1175/1520-0469(2001)058<1051:TDEIHD>2.0.CO;2.

Friedman, I., Harris, J.M., Smith, G.I., and Johnson, C.A., 2002, Stable isotope composition of waters in the Great Basin, United States 1. Air-mass trajectories: Journal of Geophysical Research, v. 107, doi: 10.1029/2001JD000565.

Galewsky, J., 2009, Orographic precipitation isotopic ratios in stratified atmospheric flows: Implications for paleoelevation studies: Geology, v. 37, p. 791–794, doi: 10.1130/G30008A.1.

Griffiths, G. A., 1981, Some suspended sediment yields from South Island catchments, New Zealand, Journal of the American Water Resources Association., v. 17, no. 4, p. 662–671, doi:10.1111/j.1752-1688.1981.tb01274.x.

Herman, F., Rhodes, E.J., Braun, J., and Heiniger, L., 2010, Uniform erosion rates and relief amplitude during glacial cycles in the Southern Alps of New Zealand, as revealed from OSL-thermochronology: Earth and Planetary Science Letters, v. 297, p. 183–189, doi: 10.1016/j.epsl.2010.06.019.

Herold, N., Huber, M., and Müller, R.D., 2011, Modeling the miocene climatic optimum. Part I: Land and Atmosphere: Journal of Climate, v. 24, p. 6353–6373, doi: 10.1175/2011JCLI4035.1.

Hicks, D. M., J. Hill, and U. Shankar, 1996, Variation of suspended sediment yields around New Zealand: The relative importance of rainfall and geology, in Erosion and Sediment Yield: Global and Regional Perspectives, edited by D. E. Walling, and B. W. Webb, IAHS Publ., 236, 149– 156.

Hong, S.-Y., Dudhia, J., and Chen, S.-H., 2004, A Revised Approach to Ice Microphysical Processes for the Bulk Parameterization of Clouds and Precipitation:

Monthly Weather Review, v. 132, p. 103–120.

Hovius, N., Stark, C.P., and Allen, P.A., 1997, Sediment flux from a mountain belt derived by landslide mapping: Geology, v. 25, p. 231–234.

Hughes, M., Hall, A., and Fovell, R.G., 2008, Blocking in Areas of Complex Topography, and Its Influence on Rainfall Distribution: Journal of the Atmospheric Sciences, v. 66, p. 508–518, doi: 10.1175/2008JAS2689.1.

Kerr, T., Srinivasan, M.S., and Rutherford, J., 2015, Stable Water Isotopes across a Transect of the Southern Alps, New Zealand: Journal of Hydrometeorology, v. 16, p. 702–715, doi: 10.1175/JHM-D-13-0141.1.

Lechler, A.R., and Galewsky, J., 2013, Refining paleoaltimetry reconstructions of the Sierra Nevada: California, using air parcel trajectories: Geology, v. 41, p. 259–262, doi: 10.1130/G33553.1.

Mulch, A., 2016, Stable isotope paleoaltimetry and the evolution of landscapes and life: Earth and Planetary Science Letters, v. 433, p. 180–191, doi: 10.1016/j.epsl.2015.10.034.

National Centers for Environmental Prediction/National Weather Service/NOAA/U.S. Department of Commerce, 2000, NCEP FNL Operational Model Global Tropospheric Analyses, continuing from July 1999, https://doi.org/10.5065/D6M043C6, Research Data Archive at the National Center for Atmospheric Research, Computational and Information Systems Laboratory, Boulder, Colo. (Updated daily.) (August 2015).

Norris, R., and Cooper, A., 2001, Late Quaternary slip rates and slip partitioning on the Alpine Fault, New Zealand: Journal of Structural Geology, v. 23.

Poage, M.A., and Chamberlain, C.P., 2001, Empirical relationships between elevation and the stable isotope composition of precipitation and surface waters: Considerations for studies of paleoelevation change: American Journal of Science, v. 301, doi: 10.2475/ajs.301.1.1.

Poage, M.A., and Chamberlain, C.P., 2002, Stable isotopic evidence for a Pre-Middle Miocene rain shadow in the western Basin and Range: Implications for the paleotopography of the Sierra Nevada: Tectonics, v. 21, doi: 10.1029/2001TC001303.

Skamarock, W.C., Klemp, J.B., Dudhi, J., Gill, D.O., Barker, D.M., Duda, M.G., Huang, X.-Y., Wang, W., and Powers, J.G., 2008, A Description of the Advanced Research WRF Version 3: NCAR Technical Note, NCAR/TN-475+STR, p. 113.

Stein, A.F., Draxler, R.R, Rolph, G.D., Stunder, B.J.B., Cohen, M.D., and Ngan, F., 2015, NOAA's HYSPLIT atmospheric transport and dispersion modeling system, Bulletin of the American Meteorological Society, v. 96, p. 2059-2077, doi: http://dx.doi.org/10.1175/BAMS-D-14-00110.1.

Sutherland, R., 1995, The Australia-Pacific boundary and Cenozoic plate motions in the SW Pacific: Some constraints from Geosat data: Tectonics, v. 14, no.4, p. 819–831.

Tippett, J.M., and Kamp, P.J.J., 1993, Fission Track Analysis of the Late Cenozoic Vertical Kinematics of Continental Pacific Crust, South Island, New Zealand: Journal of Geophysical Research, v. 98, p. 16119–16148.

Wakabayashi, J., 2013, Paleochannels, stream incision, erosion, topographic evolution, and alternative explanations of paleoaltimetry, Sierra Nevada, California: Geosphere, v. 9, p. 191–215, doi: 10.1130/GES00814.1.

Walcott, R.I., 1998, Modes of Oblique Compression: Late Cenozoic Tectonics of the Souther Island of New Zealand: Reviews of Geophysics, v. 36.

Zachos, J.C., Dickens, G.R., and Zeebe, R.E., 2008, An early Cenozoic perspective on greenhouse warming and carbon-cycle dynamics: Nature, v. 451, p. 279–283, doi: 10.1038/nature06588.

5. CONCLUSIONS AND FUTURE WORK

5.1. Conclusions

Using the relationship of decreasing δ-values and increasing elevation (Chamberlain and Poage, 2000), isotope-based paleoaltimetry seeks to quantitatively estimate the magnitude and timing of surface uplift from records of the isotopic composition of precipitation in an effort to constrain the tectonic evolution of a mountain range. This dissertation addresses the underlying assumptions in isotope-based paleoaltimetry, specifically those that are related to atmospheric dynamics. The chapters in this dissertation detail either windward or leeside isotope-based paleoaltimetry studies and both empirical and theoretically based approaches in an effort to better understand: (1) the role of atmospheric flow deflection on leeside isotope-based paleoaltimetry records and the subsequent interpretations of those records, (2) whether simple models of upslope flow are sufficient for understanding mountain-atmosphere interactions, and (3) the limitations and opportunities provided by theoretical approaches based on Rayleigh distillation.

First, for leeside isotope-based paleoaltimetry interpretations, atmospheric flow deflection cannot be ignored and the extent of atmospheric flow deflection in both modern and paleoclimates should be evaluated before interpreting leeside isotope-based paleoaltimetry records. In the southern Sierra Nevada and the Southern Alps, leeside isotope-based paleoaltimetry studies have tried to constrain the tectonic evolution of each region with differing degrees of success. Due to the 3-D nature of atmospheric flow patters in the southern Sierra Nevada, similar-to-modern flow patterns could have been achieved for elevations as low as 2 km during the Miocene and leeside isotope records may only indicate that the southern Sierra Nevada have been a longstanding topographic feature (Chapter 2). Whereas in the Southern Alps, the lack of flow deflection in both modern and paleoclimates, most likely explains why the leeside isotope-based paleoaltimetry record agrees well with other lines of geologic evidence for the timing of surface uplift and supports the proposed surface uplift of the Southern Alps at ~5 Ma (Chapter 4). Through the comparison of the two regions, we can conclude that leeside isotope-based paleoaltimetry is best applied in relatively low-lying mountain ranges with simple uplift histories, and where atmospheric flow patterns are not dominated by flow deflection.

Empirical and theoretical studies are based on longer-term averages but do not always have controls on how increasing height or changes in climate impact windward isotope lapse rates. From 3-D models of orographically enhanced precipitation in an idealized winter-time storm, I explored the limitations and opportunities of theoretical approaches based on Rayleigh distillation for windward isotope-based paleoaltimetry studies (Chapter 3). Lapse rates for both the Weather Research and Forecasting (WRF) simulations of orographically enhanced precipitation in an idealized winter-time storm and Rayleigh distillation models for the same atmospheric conditions generally decrease with increasing elevation (Chapter 3). The lapse rates from Rayleigh distillation models though, are almost always steeper due to the high precipitation efficiency. The steep lapse rates from the Rayleigh distillation models suggests that the theoretical approach may be more useful as a means of determining the minimum elevation of a mountain range and the maximum amount of uplift.

5.2. Future Work

The tools and methods in this dissertation expand on the previous work of Galewsky (2009, 2008) and Lechler and Galewsky (2013) and provide a framework for evaluating both leeside and windward isotope-based paleoaltimetry interpretations and techniques in different settings. Current and future studies using leeside isotope-based paleoaltimetry should use methods similar to those in Chapters 2 and 4 and Lechler and Galewsky (2013) to determine whether or not flow patterns in the region of interest are dominated by atmospheric flow deflection.

While it is recognized that the work in Chapter 3 may not be representing all the complexity of the isotopic system in the model, it is a first step to comparing lapse rates from Rayleigh distillation to orographically enhanced flow and determining what controls windward isotopic lapse rates. The work in Chapter 3 could be expanded to explore the inclusion of more complex isotope microphysics, higher resolution, more complex topography, and longer time periods that capture both summer and winter precipitation. Expanding the work in Chapter 3 would help to determine how simulated windward lapse rates change with increasing complexity and whether Rayleigh distillation models may capture the increased complexity. A deeper understanding of the processes that control windward lapse rates has the potential to improve the reliability of isotope-based paleoaltimetry interpretations used to constrain the topographic and tectonic evolution of mountain ranges.

5.3. References in Chapter 5

Chamberlain, C.P., and Poage, M.A., 2000, Reconstructing the paleotopography of mountain belts from the isotopic composition of authigenic minerals: Geology, v.

28, p. 115–118, doi: 10.1130/0091-7613(2000)28<115:RTPOMB>2.0.CO.

Galewsky, J., 2008, Orographic Clouds in Terrain-Blocked Flows: An Idealized Modeling Study: Journal of the Atmospheric Sciences, v. 65, p. 3460–3478, doi: 10.1175/2008JAS2435.1.

Galewsky, J., 2009, Orographic precipitation isotopic ratios in stratified atmospheric flows: Implications for paleoelevation studies: Geology, v. 37, p. 791–794, doi: 10.1130/G30008A.1.

Lechler, A.R., and Galewsky, J., 2013, Refining paleoaltimetry reconstructions of the Sierra Nevada: California, using air parcel trajectories: Geology, v. 41, p. 259–262, doi: 10.1130/G33553.1.

6. SUPPLEMENTAL MATERIALS

6.1. Supplemental Materials for Chapter 2

6.1.1. Pre-Industrial and Miocene Simulations

The middle Miocene is thought to be significantly warmer than modern climate (Zachos et al., 2008). We calculated annual averages of precipitation and temperature for both the Miocene and Pre-Industrial (PI) simulations of climate from 50 consecutive years. Results from the simulated Miocene climate show a global increase in temperature of 4.6°C and a global increase in precipitation of 150 mm relative to the PI simulation. The Miocene temperature increase relative to the PI simulation is in line with the 5-6 °C temperature excursion from deep ocean benthic oxygen isotopes for 17-14.5 Ma (Zachos et al., 2008). Temperature and precipitation proxies for western North America suggest that the region was both warmer and wetter than modern climate (White and Auger, 1994; Wolfe 1994a; Wolfe 1994b; Sheldon, 2006; Retallack, 2004). The Miocene simulation captures both an increase in temperature and precipitation for western North America relative to the PI simulation (Figure 6.1, Figure 6.2, Figure 6.3, Figure 6.4).

6.1.2. Simulations of Flow around Idealized Terrain

Using the Weather Research and Forecasting (WRF) model version 3.5.1 (Skamarock et al., 2008) we ran two sets of simulations for various topographic and climatic states to determine how stable a climate is needed in order for the 2-D assumptions used in the leeside proxies to faithfully record the elevation of both a high and low southern Sierra Nevada. The initial conditions for these two simulations are outlined in Table DR1 and Table DR2.

6.1.3. Modern Nh/U Calculation

We calculated N_m from five consecutive years (1995-1999) of 3-hourly North American Regional Reanalysis (NARR) output (http://www.esrl. noaa.gov/psd/). N_m was calculated for the windward region of the Sierra after Durran and Klemp (1982). We find that the average $N_m = 0.0086\ s^{-1}$ with an average modern Nh/U of 2.2. Using the 10^{th} percentile N_m, where $N_m = 0.0071\ s^{-1}$, $Nh/U = 1.8$. For our calculations of Nh/U we use $h = 3$ km.

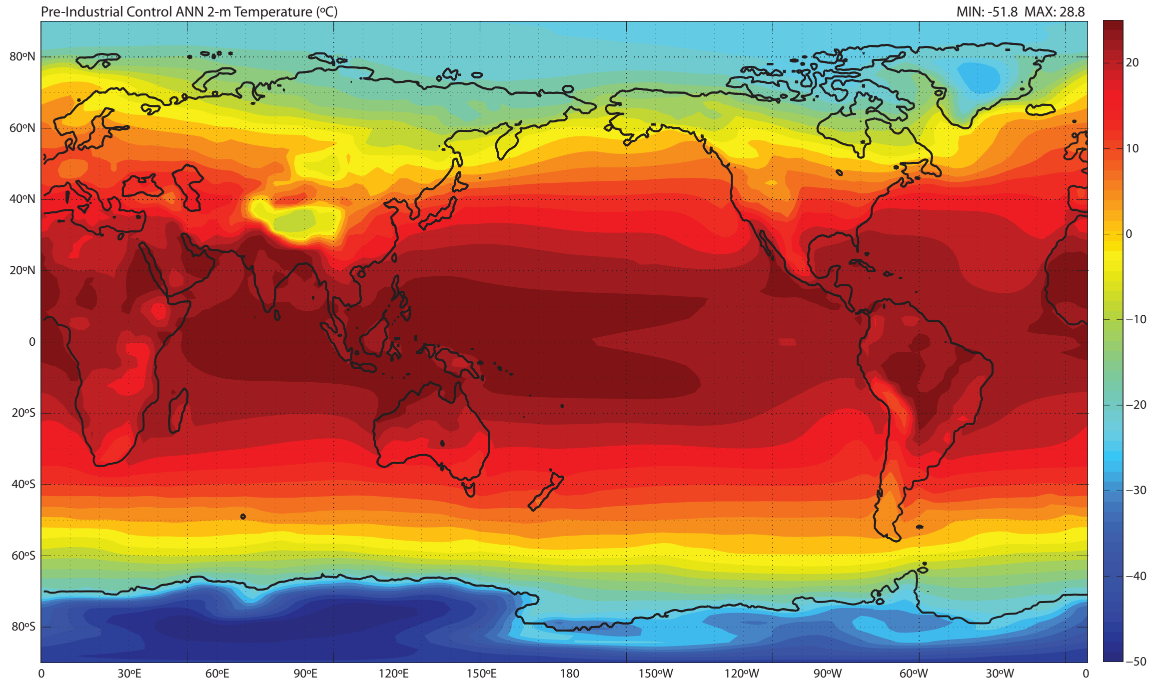

Figure 6.1. Pre-Industrial simulation annual surface temperatures (°C). The black line is the modern land-ocean boundary.

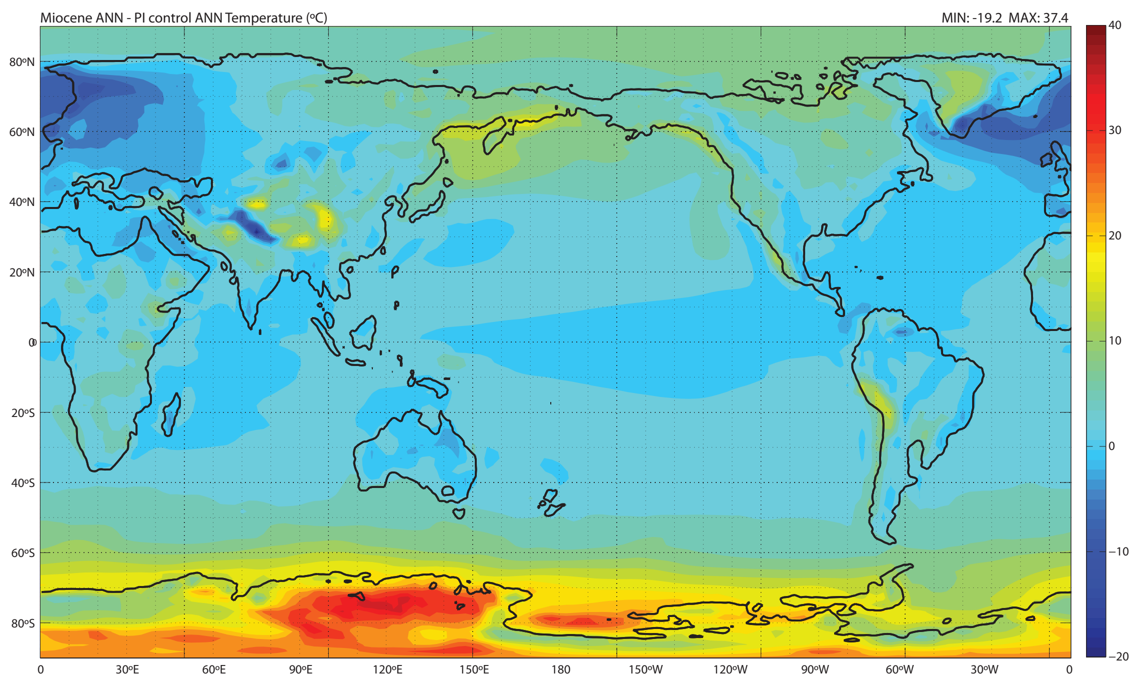

Figure 6.2. Miocene minus the Pre-Industrial simulation annual surface temperature anomaly (°C). Black contour is the Miocene land-ocean boundary.

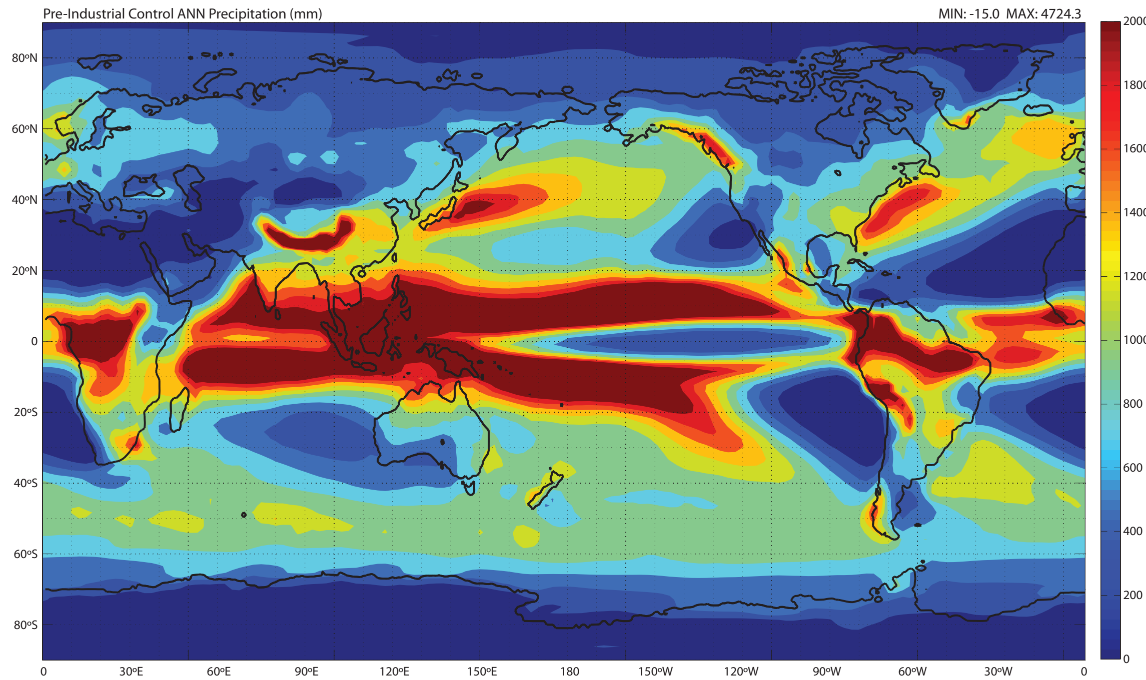

Figure 6.3. Pre-Industrial simulation annual average precipitation (mm). The black line is the modern land-ocean boundary.

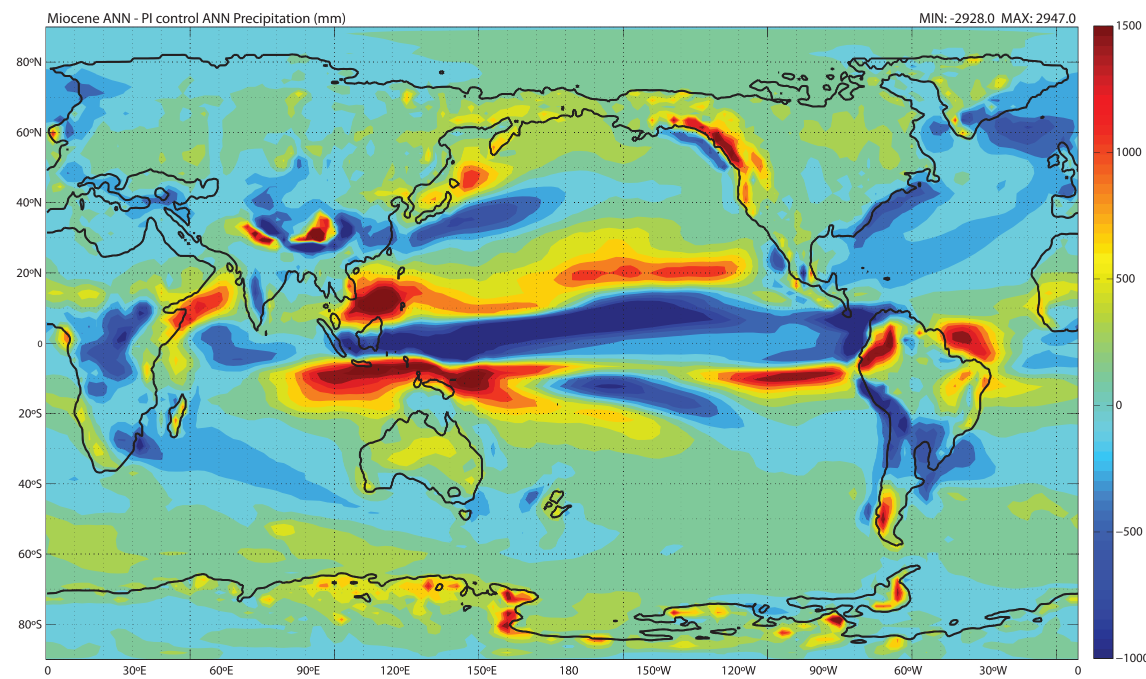

Figure 6.4. Miocene minus the Pre-Industrial simulation annual precipitation anomalies (mm). Black contour is the Miocene land surface boundary.

Experiment	Brunt-Vaisala frequency (1/s)	*Nh/U*
High_SSN_01	0.0025	0.80
High_SSN_02	0.0038	1.10
High_SSN_03	0.0049	1.50
High_SSN_04	0.0058	1.75
High_SSN_05	0.0061	1.80
High_SSN_06	0.0075	2.30
High_SSN_07	0.01	3.00

Table 6.1. Initial conditions for simulations of idealized flow for an idealized high southern Sierra Nevada.

Experiment	Brunt-Vaisala frequency (1/s)	Maximum Ridge Height (m)
LowRidge_01	0.0032	500
LowRidge_02	0.0032	1000
LowRidge_03	0.0032	1500
LowRidge_04	0.0032	2000
LowRidge_05	0.0032	2500
LowRidge_06	0.0032	3000
LowRidge_07	0.0032	3500
LowRidge_08	0.0075	2000

Table 6.2. Initial conditions for simulations of idealized flow for a uniform ridge increasing in elevation.

6.1.4. References in Chapter 6.1

Gent, P. R. et al., 2011, The Community Climate System Model Version 4, Journal of Climate, v. *24*(19), p. 4973–4991.

Durran, D.R., and Klemp, J.B., 1982, On the Effects of Moisture on the Brunt-Vaisala Frequency: J. Atmos. Sci., v. 39, p. 2152–2158.

Retallack, G.J., 2004, Late Miocene climate and life on land in Oregon within a context of Neogene global change: Palaeogeography, Palaeoclimatology, Palaeoecology, v. 214, p. 97–123.

Sheldon, N.D., 2006, Using paleosols of the Picture Gorge Basalt to reconstruct the middle Miocene climatic optimum: PaleoBios, v. 26, p. 27–36.

Skamarock, W.C., Klemp, J.B., Dudhi, J., Gill, D.O., Barker, D.M., Duda, M.G., Huang, X.-Y., Wang, W., and Powers, J.G., 2008, A Description of the Advanced Research WRF Version 3: NCAR Technical Note, v. Tech. Note, p. 113.

White, J. M., and T. A. Ager, 1994: Palynology, paleoclimatology and correlation of Middle Miocene beds from Porcupine River (locality 90-1), Alaska. Quat. Int., 22–23, 43–77.

Wolfe, J. A., 1994a: Tertiary climatic changes at middle latitudes of western North America. Palaeogeogr., Palaeoclimatol., Paleoecol., 108, 195–205.

Wolfe, J. A., 1994b: An analysis of Neogene climates in Beringia. Palaeogeogr., Palaeoclimatol., Paleoecol., 108, 207–216.

Zachos, J.C., Dickens, G.R., and Zeebe, R.E., 2008, An early Cenozoic perspective on greenhouse warming and carbon-cycle dynamics.: Nature, v. 451, p. 279–283.

6.2. Supplemental Materials for Chapter 3

6.2.1. Control Simulation Validation

For the purpose of validation and comparison to other models of baroclinic waves we run a control simulation with no topography for 15 days. We compare our results to Dütsch et al. (2016). Dütsch et al. (2016) used the COSMOiso model to simulate an idealized baroclinic wave. COSMOiso includes the heavy isotopes, δD and $\delta^{18}O$, and fractionation takes place upon any phase transition. This differs from our model where fractionation only takes place upon condensation. While the isotope scheme in COSMOiso is more sophisticated, our results from a control simulation without any topography show a similar spatial distribution and magnitude of change in the isotopic composition of precipitation.

Unlike the other simulations presented here, the initial δD_{vapor} of our control simulation is uniform throughout the atmosphere and is set at -100 ‰ vSMOW. The model presented here from Dütsch et al. 2016 uses an initial δD_{vapor} of -80 ‰ vSMOW.

Here we show the modeled precipitation and resulting $\delta D_{precipitation}$ from our control simulation at 186 hours (Figure 6.5) and for the model from Dütsch et al. (2016) we show the $\delta D_{precipitation}$ at 108 hours (Figure 6.6). The structure of the precipitation is not exactly the same because the two models are different in resolution, domain size, initial conditions and isotope scheme but broadly, the baroclinic wave simulation from the Weather Research and Forecasting model (WRF) has the same shape and the magnitude of change for the 6 hourly precipitation (Figure 6.5 and Figure 6.6). For the WRF simulation there is an ~120 ‰ difference across the precipitation and in Dütsch et al. (2016) there is an ~150 ‰ difference across the precipitation. Our simulation is initialized with a lower $\delta D_{vapor,}$ so it is not surprising that the Dütsch et al. (2016) have a greater variation in $\delta D_{precipitation}$.

While the isotope scheme in COSMOiso is more sophisticated, our results from a control simulation without any topography show a similar spatial distribution and magnitude of change in the isotopic composition of precipitation. This leads us to believe that our model is capturing the first-order controls on the isotopic composition of the precipitation.

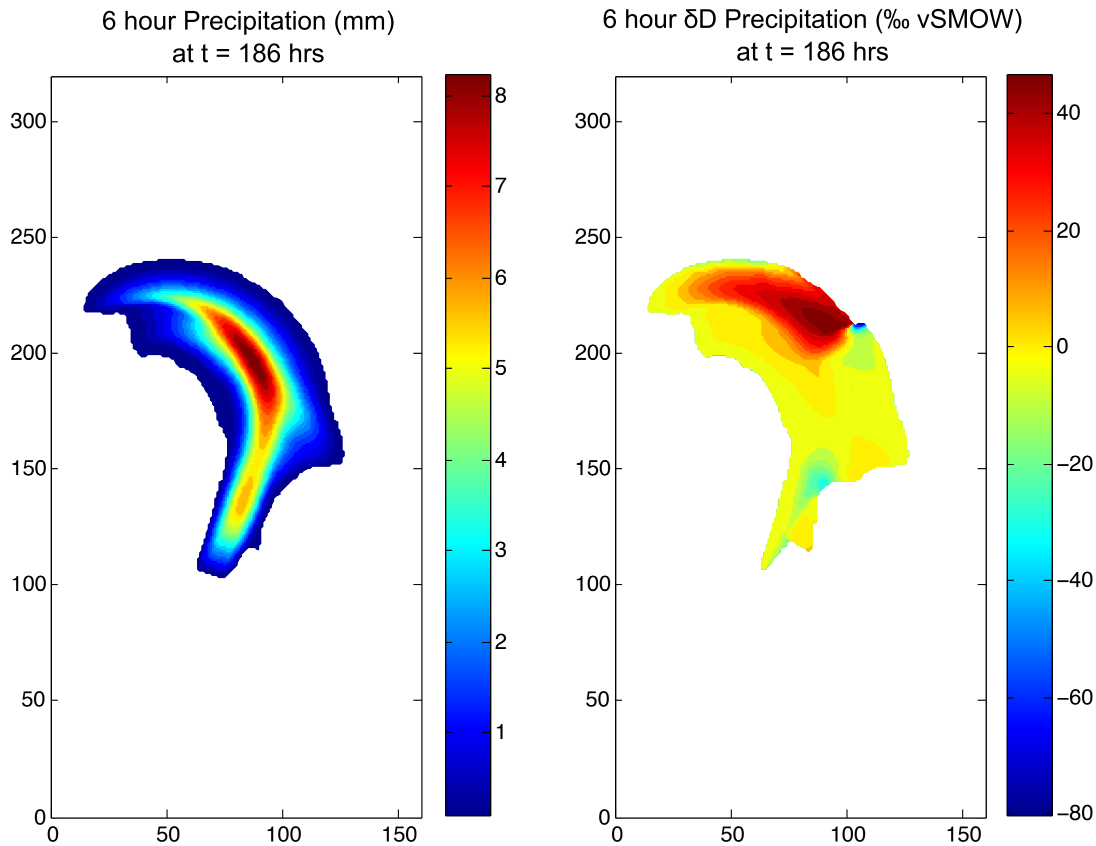

Figure 6.5. 6 hour precipitation and $\delta D_{precipitation}$ at t = 186 hours for the control simulation. Precipitation is in mm and the $\delta D_{precipitation}$ is in ‰ vSMOW.

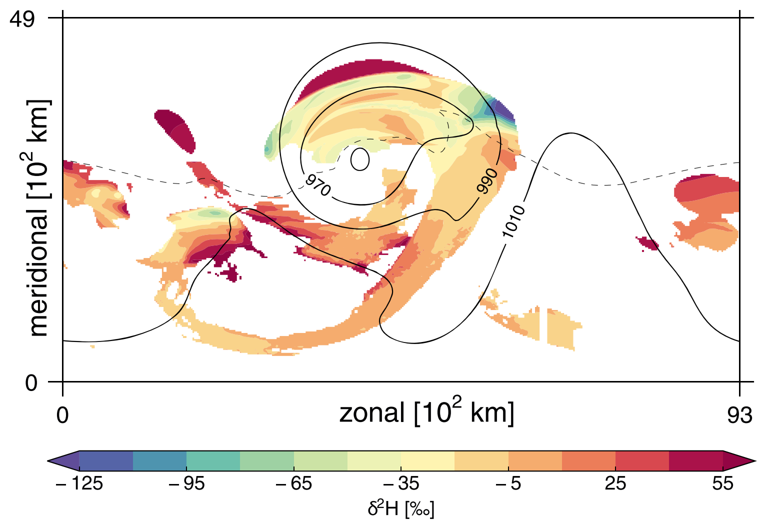

Figure 6.6. Surface precipitation for their simulation with uniform initial δD_{vapor} (Figure from Dütsch et al., 2016). The solid black lines show sea level pressure in hPa, and the dashed line is the 0˚C isoline of temperature at the lowest model level.

6.2.2. High Resolution Simulation

To test the influence of resolution on the results of our model, we ran a 10 km resolution simulation with a 2.5 km ridge. Due to computational time, we only ran the 10 km resolution simulation for 8.5 days and only directly compare from day 6 to 8.5. For the 25 km resolution simulation we find that the lapse rate for the model is -8.3 ‰/km and that the lapse rate is slightly lower at -6.2 ‰/km from day 6 to 8.5. For the 10 km resolution simulation we find that the lapse rate is -6.3 ‰/km. This is similar to the 25 km resolution simulation. The $\delta D_{precipitation}$ is for the 10 km resolution simulation is 10 ‰ greater than in the 25 km resolution simulation from day 6 to 8.5. The simulated WRF lapse rates are very similar between the high and low resolution simulations despite the increase in $\delta D_{precipitation}$ for the higher resolution simulation.

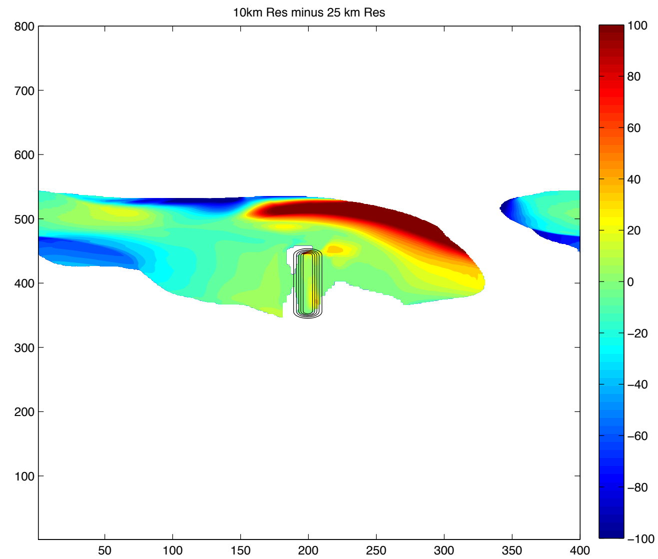

Figure 6.7. Difference in cumulative $\delta D_{precipitation}$ from day 6 to day 8.5 for the 2.5 km ridge simulation. Black contours are the elevation of the ridge with 500 m contour intervals.

6.2.3. References in Chapter 6.2

Dütsch, M., Pfahl, S., and Wernli, H., 2016, Drivers of δ^2H variations in an idealized extratropical cyclone: Geophysical Research Letters, v. 43, p. 5401–5408, doi: 10.1002/2016GL068600.1.